AUBURN ENGINEERING

Investigation of Thermal Creep and Thermal Stress Effects in Microgravity Physical Vapor Transport

Contract NASA–NAG8–977

Final Report

D.W. Mackowski, PI
R. W. Knight, Co–I

Mechanical Engineering Department
College of Engineering
Auburn University, AL 36849

Contract Period: 8/1/93–1/31/96

Dr. Benjamin G. Penn, Technical Officer
ES74, George C. Marshall Space Flight Center

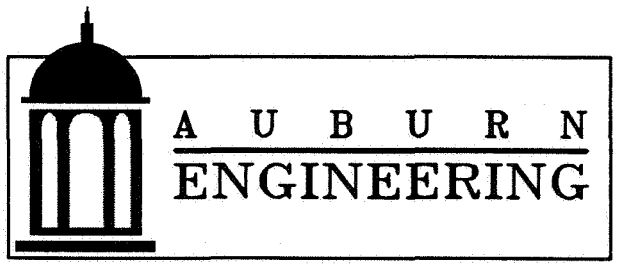

Investigation of Thermal Creep and Thermal Stress Effects in Microgravity Physical Vapor Transport

Contract NASA–NAG8–977

Final Report

D.W. Mackowski, PI
R. W. Knight, Co–I

Mechanical Engineering Department
College of Engineering
Auburn University, AL 36849

Contract Period: 8/1/93–1/31/96

Dr. Benjamin G. Penn, Technical Officer
ES74, George C. Marshall Space Flight Center

1. Report Summary

Reported here are the results of our numerical investigation into the mechanisms which affect the transport and growth processes in Physical Vapor Transport (PVT) crystal growth ampoules. The first part of the report consists of a brief summary of the major accomplishments and conclusions of our work. The second part consists of two manuscripts, submitted to the *Journal of Crystal Growth*, which provided a detailed description of the findings in our investigation.

2. Project Objectives

The objectives of the project were to conduct a detailed numerical examination of the vapor transport mechanisms which govern the growth of crystals in PVT ampoules. A specific focus of the project was to examine the effects of thermal creep and thermal stress convection on the crystal growth process. These mechanisms result from temperature gradients along the solid surfaces of the system (thermal creep) and within the bulk gas (thermal stress). Typically, the convective velocities resulting from thermal creep and stress are significantly smaller than those resulting from buoyant convection under similar nonisothermal conditions in normal gravity. However, in microgravity conditions the creep and stress mechanisms could potentially have a significant effect on vapor transport relative to diffusion–limited conditions.

A second focus of the project, which was developed subsequent to the initial proposal, involved the examination of the effects of conduction heat transfer within the solid crystal, and deposition of the vapor onto the side wall the ampoule, on crystal growth rates and growth uniformity.

3. Effect of Thermal Creep and Stress on PVT

Thermal creep is a slip flow of gas over a solid surface which results from a temperature gradient tangential to the surface. On a phenomenological basis, the thermal creep velocity is given by

$$u_C = \frac{C_s \nu}{T} \left. \frac{\partial T}{\partial z} \right|_{wall}, \tag{1}$$

where ν is the kinematic viscosity of the gas, z is the coordinate tangential to the wall, and C_s is a dimensionless coefficient, of order unity, which depends on the momentum and thermal accommodation of the molecule–wall collisions. In ampoules with nonisothermal side walls, thermal creep would result in a recirculating flow within the ampoule. The gas would slip along the side walls towards the higher–temperature source, and return along the centerline to the lower–temperature crystal.

To examine the effects of creep–induced recirculation, we first developed a numerical

model to predict the vapor growth rates in PVT ampoules. The model consisted of a steady–state, two–dimensional axisymmetric representation of a binary component (nutrient + inert carrier) PVT system. A fully compressible formulation was employed in the formulation of the governing continuity, momentum, energy, and species equations. Along with thermal creep and natural convection, the model included transport of nutrient by Soret diffusion. To facilitate the identification of regimes in which thermal creep had a significant effect on growth rates, a non–dimensional formulation of the governing equations was adopted.

Details of the formulation and calculation results appear in Mackowski et al. (1996b) (given in Appendix A). We found that thermal creep will have a significant effect on the distribution of mass flux at the crystal interface only for relatively large Schmidt number ($Sc = \nu/D_{AB}$, where ν and D_{AB} are the kinematic viscosity and binary diffusion coefficient) conditions, and relatively large wall temperature gradients adjacent to the crystal interface. Such conditions, however, have been realized in a number of ground and space–based PVT experiments, in particular those involving systems containing a trace concentration of a large molecular mass nutrient in a low molecular mass carrier (such as the 3M PVTOS experiments).

The overall effect of thermal creep convection on crystal growth is qualitiatively similar to that resulting from buoyant convection. Thermal creep creates a recirculating flow within the ampoule, with the fluid driven along the ampoule walls from the lower–temperature crystal to the higher–temperature source, and returning to the crystal along the ampoule centerline. The recirculation augments the deposition rate at the crystal surfaces nearest the centerline, and retards the growth rates near the side wall. Variations in mass flux of up to 50% in the presence of thermal creep were identified for realistic PVT growth parameters, as opposed to essentially uniform mass flux for creep and buoyancy–free conditions for the same operating parameters.

Even in systems where the absolute difference in the source and crystal temperatures is not large, relatively large wall temperature gradients adjacent to the crystal can occur as a result of wall heating strategies that are used to control parasitic nucleation on the walls. In conjunction with thermal creep, these gradients can lead to gas recirculation patterns directly above the crystal interface, which in turn can result in a distribution of flux at the interface that is significantly more nonuniform than that predicted in the absence of creep.

We also performed a limited number of calculations that included the convection mechanism of thermal stress. Thermal stress is predicted from the Burnett contributions to the fluid stress tensor – which constitute the second–order approximation to the Boltzmann equation for small Knudsen flows (the Navier–Stokes equations being the first order ap-

proximation). These constituitive relations predict that a non–linear temperature gradient in the fluid gas can directly impart a fluid stress, and lead to a bulk convection of the fluid.

Our predictions indicate that 1) thermal stress convection is only significant for extremely high temperature gradient conditions (i.e., $\sim$ 100 K/cm), and 2) the thermal creep flows generated from these temperature gradients invariably overwhelm the thermal stress flows. Consequently, in regard to crystal growth, we do not believe that conditions exist in which thermal stress, by itself, would have an appreciable effect on the growth rates and morphology of the crystal. However, the thermal stress flows that we have predicted are intriguing in themselves. Under earthbound conditions thermal stress convection in nonisothermal gases will be insignificant compared to buoyant convection. The μg environment, on the other hand, offers conditions in which thermal stress convection could become a significant if not dominant mode of convection in nonisothermal gases. Our future work will focus on thermal stress convection in single–component (i.e., no mass transfer), near–continuum gases, with the goal of identifying designs for microgravity–based experiments to measure thermal stress convection in nonisothermal gases.

4. Effect of solid–phase heat transfer and wall deposition

Previous PVT numerical modelling efforts (including those discussed above) have taken the crystal interface to be planar and isothermal. In reality, conduction heat transfer through the solid, coupled with the latent heat release of the depositing crystal, can lead to nonuniformities in the crystal surface temperature. This, in turn, will affect the saturation partial pressure of the nutrient above the crystal and thus alter the arriving flux. In addition, parasitic nucleation on the side walls of the ampoule can lead to a growth interface that, overall, is non–planar.

To examine these issues, we modified our numerical model of the PVT system to include conduction heat transfer in the crystal and deposition of the nutrient on the side walls. Details of the investigation appear in Mackowski (1996a) (Appendix B). The results show that solid phase heat transfer, combined with the latent heat release from the depositing vapor, can significantly retard the overall growth rates in PVT systems. The predicted transport conditions under which heat transfer has a controlling role on crystal growth are consistent with a simplified, one–dimensional analysis of combined heat and mass transfer in PVT ampoules. The effect of heat transfer on the surface temperature distribution of the crystal is strongly dependent on the thermal boundary conditions at the side surfaces of the crystal substrate. Adiabatic conditions promote one–dimensional heat transfer, which leads to nearly isothermal surface temperature distributions and uniform growth rates. Cooled side walls, on the other hand, can lead to highly nonuniform surface temperature distributions, and correspondingly nonuniform growth rates.

Deposition of the crystal vapor onto the ampoule walls can have an equally significant effect on the flux distribution. The redirection of vapor to the side walls has the primary effect of scavenging vapor from the crystal interface, which results in an overall decrease in mass transfer to the interface and a highly nonuniform flux distribution. For certain PVT conditions, our results also indicate that wall deposition can lead to buoyant recirculation even when the ampoule is oriented in a convectively 'stable' configuration. This phenomenon can result in interface flux distributions that are significantly different than those obtained under buoyancy–free, zero gravity environments for the same model conditions.

5. Project Bibliography

1. D. G. Walker, D. W. Mackowski, and R. W. Knight, "Effect of thermal creep on physical vapor transport crystal growth," AIAA 32nd Aerospace Sciences Meeting and Exhibit, 10–13 January 1994, Reno, NV, paper 94–0567.
2. D. W. Mackowski and R. W. Knight, "Numerical Modelling of Physical Vapor Transport under Microgravity Conditions: Effect of Thermal Creep and Stress," in *Microgravity Studies of Organic and Polymeric Materials*, D.O. Frazier and C.E. Moore, Eds., NASA Conference Publication 3250, pp. 17–20 (1994).
3. D. W. Mackowski, R. V. Rao, and R. W. Knight, "Effect of solid phase heat transfer and wall deposition on crystal growth in physical vapor transport ampoules," *J. Crystal Growth*, accepted for publication (1996).
4. D. W. Mackowski, R. V. Rao, D. G. Walker, and R. W. Knight, "Numerical investigation of the effects of thermal creep in physical vapor transport," *J. Crystal Growth*, submitted for publication (1996).

6. Supported Personnel

1. D. G. Walker (MS, 1994)
2. V. R. Rao (Postdoctoral Research Associate)

Appendix A

Numerical Investigation of the Effects of Thermal Creep in Physical Vapor Transport

D.W. Mackowski, V.R. Rao, D.G. Walker and R.W. Knight

Mechanical Engineering Department

Auburn University, AL 36849

Submitted to *J. Crystal Growth*, 2/96

Abstract

It has been recently recognized that the nonisothermal conditions present in physical vapor transport ampoules can give rise to a slip flow of gas over the side walls of the ampoule. This phenomenon, known as thermal creep, is usually insignificant relative to buoyancy–induced flows under similar nonisothermal conditions, and has therefore been neglected in previous PVT numerical models. However, thermal creep can, in principle, become a dominant convection mechanism in buoyancy–free environments such as those encountered in microgravity experiments. We present here a numerical investigation of the effects of thermal creep on the growth process in axisymmetric, binary component PVT systems. A nondimensional model, which includes buoyancy and Soret diffusion, is developed. We show that thermal creep can result in recirculating bulk flows within the ampoule. For relatively high values of the Schmidt number and large wall temperature gradients, these flows can result in significantly nonuniform distributions of mass flux at the crystal interface, and can also be comparable to or exceed the flow velocities generated by buoyancy under normal gravities. The effects of thermal creep on buoyant convection, and on the Soret transport of the vapor, are examined.

1. Introduction

The formation of crystal structures is largely governed by the mass transport of the fluid material as it crystallizes at the nutrient/crystal interface [1]. This is certainly the case in physical vapor transport (PVT) crystal growth processes. In general, PVT is the process in which an amorphous solid is vaporized at one end of a closed, cylindrical ampoule, transported across the ampoule (usually through an inert carrier gas), and deposited onto a substrate that is maintained at a lower temperature than the source. The temperature and/or composition gradients that are invariably present in PVT processes can result in vapor transport that is dominated by buoyancy–induced convection. However, under microgravity (μg) environments the driving force behind buoyancy is largely eliminated and vapor transport occurs ostensibly in a diffusion–limited mode. Indeed, crystals grown in μg PVT experiments have been shown to posess uniquely different and improved structural properties that those grown on earth under similar operating conditions [2–4]. It is not known, however, to what extent the improvements result from modified vapor–phase transport conditions or the reduction in weight strain within the crystal.

Because of the considerable cost in performing μg PVT experiments, much effort has been given to numerical modelling of the process. Markham and Rosenberger [5] were the first to numerically examine the effects of microgravity on vapor transport rates in a cylindrical ampoule. Their results demonstrated that, under μg conditions, the transport of vapor is not adequately described by one–dimensional diffusion of the nutrient through a stagnant carrier fluid. Rather, the rejection of the carrier at the source and crystal interfaces leads to a recirculation of the carrier within the ampoule, which in turn results in radial concentration gradients of the nutrient. The effect of carrier recirculation and buoyant recirculation on growth rates and growth uniformity have been further examined in comprehensive numerical investigations of PVT by Greenwell [6], Markham et al. [7], and Nadarajah et al. [8].

In general, a key conclusion of the previous modelling efforts is that the elimination of buoyancy–induced convection results in improved uniformity of growth at the crystal interface. Recently, however, Rosner [9] reported that the non–isothermal conditions encountered in PVT processes can lead to additional, previously–unrecognized convection mechanisms. In particular, a temperature gradient tangential to a wall can result in a slip flow of gas over the wall. This phenomemon, which is known as thermal creep, is a macroscopic consequence of the molecular transfer of momentum to the wall. Molecules originating from the warmer regions in the gas will strike a wall with a higher momentum than those arriving from the cooler regions. The surface reacts to this uneven momentum transfer by imparting a force in the gas that is directed towards the warmer regions, which results in a slip flow over the surface.

The velocity of the creep flow is phenomenologically related to the temperature gradient by [9–11]

$$u_C = \frac{C_s \nu}{T} \left. \frac{\partial T}{\partial z} \right|_{wall}, \tag{1}$$

where ν is the kinematic viscosity of the gas, z is the coordinate tangential to the wall, and C_s is a dimensionless coefficient which depends on the momentum and thermal accommodation of the molecule–wall collisions. For diffuse reflection of the molecules the value of C_S is estimated as 2.2 [10]. Under normal gravity conditions thermal creep typically results in a velocity that is significantly smaller than buoyancy–induced velocities produced under similar nonisothermal conditions, and has therefore been neglected in practically all numerical investigations of earthbound heat and mass transfer processes. In vanishing gravity, however, Rosner qualitatively indicated that the creep velocity can become comparable to the typical Fickian diffusion velocity in PVT processes [9]. His conclusions were further supported by order-of–magnitude analyses by Napolitano et al. [12] and Viviani et al. [13].

To summarize these previous qualitative analyses, note first that the characteristic Stefan velocity of the vapor will be given by $u_D = D_{AB} Pe/L$, where D_{AB} is the binary diffusion coefficient, L is the ampoule length, and Pe is the mass transfer Peclet number based on the mass–averaged velocity. Assuming that the ampoule wall temperature varies linearly from the source temperature T_S to the crystal temperature T_C, the characteristic creep velocity u_c at the crystal is obtained from Eq. (1) as $u_C \approx \nu C_s (T_S - T_C)/LT_C$. Consequently, the ratio of the characteristic creep and Stefan velocities is

$$\frac{u_c}{u_D} \approx \frac{\nu C_s}{PeD_{AB}} \frac{T_S - T_C}{T_C} = \frac{Sc\, C_s \Delta T^*}{Pe}, \tag{2}$$

in which $Sc = \nu/D_{AB}$ is the Schmidt number and ΔT^* is a characteristic nondimensional temperature difference. Considering the fact that ΔT^* cannot realistically exceed values of around 0.5 (and will most likely be around 0.05–0.1), the creep and Stefan velocities will be comparable only for conditions of large Sc/Pe. This condition will be attained for vanishing concentration of the nutrient in the carrier ($Pe \ll 1$) and, simultaneously, relatively large ratios of the molecular weights of the nutrient and carrier (large Sc). As noted in Refs. [9, 12, 13], there have been a number of μg experiments that fall into this regime – most notably the copper phthalocyanine experiments of Debe et al. [3].

The objective of this work is to use detailed numerical modelling to quantitfy the effects of thermal creep on the PVT process. Since the conditions that are favorable to creep flows (i.e., large Sc and/or ΔT^*) are also the conditions in which Soret (i.e., thermal) diffusion can become important, a second objective of the work is to examine the role of Soret diffusion (in combination with thermal creep) on vapor transport. Emphasis is given

to the effect of these transport mechanisms on the growth rates and growth uniformity at the crystal interface, and the differences in the growth patterns that occur with and without buoyancy.

2. Transport Model

The geometry of the PVT ampoule is schematically illustrated in Fig. 1. The ampoule is cylindrical, with length L and radius R. Nutrient vapor, denoted as species A, originates from a planar source at $z = 0$ and deposits onto a planar crystal at $z = L$. The source and crystal interfaces are taken to be stationary, which is appropriate for the highly disparate vapor and solid phase densities of the nutrient. We also neglect the effects of heat transfer within the source and crystal, and take both surfaces to be at the uniform temperatures of T_S and T_C, respectively. A constant mass of carrier gas, denoted as species B, resides within the ampoule and is completely rejected at all surfaces. The system is axisymmetric, in steady–state, and all transport properties of the gas mixture are assumed constant.

To facilitate the identification of regimes in which creep and Soret mechanisms contribute to vapor transport, we adopt a nondimensional formulation of the governing equations. The velocities are normalized by the characteristic diffusion velocity D_{AB}/L, the temperature, pressure, and density of the gas are normalized by the values at the source, and the position variables are normalized with the ampoule length L. Denoting the nondimensional variables with the superscript $*$, the equations for mass, momentum, energy, and species conservation become

$$\frac{1}{r^*}\frac{\partial(\rho^* r^* v^*)}{\partial r} + \frac{\partial(\rho^* u^*)}{\partial z^*} = 0 \tag{3}$$

$$\frac{1}{r^*}\frac{\partial(\rho^* r^* v^* v^*)}{\partial r^*} + \frac{\partial(\rho^* u^* v^*)}{\partial z^*} = -N_P\frac{\partial P^*}{\partial r^*} + Sc\left[\frac{2}{r^*}\frac{\partial}{\partial r^*}r^*\frac{\partial v^*}{\partial r^*} - \frac{2}{3}\frac{\partial}{\partial r^*}\nabla\cdot\mathbf{v}^* + \frac{\partial}{\partial z^*}\left(\frac{\partial v^*}{\partial z^*} + \frac{\partial u^*}{\partial r^*}\right) - \frac{2v^*}{r^{*2}}\right] \tag{4}$$

$$\frac{1}{r^*}\frac{\partial(\rho^* r^* u^* v^*)}{\partial r^*} + \frac{\partial(\rho^* u^* u^*)}{\partial z^*} = -N_P\frac{\partial P^*}{\partial z^*} + Sc\left[\frac{1}{r^*}\frac{\partial}{\partial r}r^*\left(\frac{\partial v^*}{\partial z^*} + \frac{\partial u^*}{\partial r^*}\right) + 2\frac{\partial}{\partial z^*}\left(\frac{\partial u^*}{\partial z^*} - \frac{1}{3}\nabla\cdot\mathbf{v}^*\right)\right] + \rho^* g^* \tag{5}$$

$$\frac{1}{r^*}\frac{\partial(\rho^* r^* v^* T^*)}{\partial r^*} + \frac{\partial(\rho^* u^* T^*)}{\partial z^*} = \frac{Sc}{Pr}\left(\frac{1}{r^*}\frac{\partial}{\partial r^*}r^*\frac{\partial T^*}{\partial r^*} + \frac{\partial^2 T^*}{\partial z^{*2}}\right) \tag{6}$$

$$\frac{1}{r^*}\frac{\partial(\rho^* r^* v^* w)}{\partial r^*} + \frac{\partial(\rho^* u^* w)}{\partial z^*} = -\nabla\cdot\rho^*\mathbf{v}_A^*. \tag{7}$$

In the above, u^* and v^* denote the z and r components of the nondimensional mass

averaged velocity, and w is the mass fraction of the nutrient. The dimensionless parameters appearing in the momentum equations are defined

$$N_P = \frac{P_S L^2}{\rho_S D_{AB}^2}, \quad g^* = \frac{gL^3}{D_{AB}^2}, \tag{8}$$

in which subscript S refers to the value at the source, and $Pr = c_p\mu/k$ is the Prandtl number of the mixture. Note that the Schmidt number is defined with respect to the density at the source, i.e., $Sc = \mu/\rho_S D_{AB}$, and the Rayleigh number for expansive/solutal buoyant convection is $Ra_L = |(1 - \rho_C/\rho_S)g^*|/Sc$. The nondimensional diffusion velocity of the nutrient, $\mathbf{v}_A^*$, is comprised of Fickian and Soret components via

$$\mathbf{v}_A^* = -\nabla w - \alpha_T \frac{w(1-w)}{T^*}\nabla T^*, \tag{9}$$

in which α_T denotes the Soret (or thermal diffusion) factor [1, 14]. The corresponding cross–product transport mechanism in the energy equation, i.e., Dufour diffusion (enthalpy diffusion via a concentration gradient), has been neglected – which will be appropriate for the Pr/Sc conditions of interest. Likewise, we have neglected the contribution of temperature gradients to fluid stress ('thermal stress') in the momentum equations. Based on the order–of–magnitude estimates in Refs. [12, 13], this mechanism will not significantly affect the flow field for the conditions examined here.

We assume ideal behavior of the gas in the ampoule. We also neglect the effects of flow–induced pressure gradients on the gas density – which is entirely reasonable for the low Reynolds number conditions of typical PVT systems. The density will then be a function solely of temperature and composition. In nondimensional form, the ideal gas law will then become

$$\rho^* = \frac{M^*}{T^*}, \tag{10}$$

with a nondimensional molecular mass of the mixture, M^*, given by

$$M^* = \frac{M}{M_S} = \frac{w_S(1 - N_M) + N_M}{w(1 - N_M) + N_M}, \tag{11}$$

where $N_M = M_A/M_B$ is the ratio of molecular masses of the nutrient and carrier.

Infinite–rate deposition kinetics are assumed at the source and crystal interfaces, which will correspond to fixed mole fractions of the nutrient at the interfaces for a given total pressure. The boundary conditions at the source are then

$$T^*(r^*, 0) = 1 \tag{12}$$

$$w(r^*, 0) = \frac{N_M x_S}{1 + (N_M - 1)x_S} \tag{13}$$

$$v^*(r^*, 0) = 0 \tag{14}$$

$$u^*(r^*, 0) = -\frac{1}{1-w}\left(\frac{\partial w}{\partial z^*} + \frac{\alpha_T w}{T^*}\frac{\partial T^*}{\partial z^*}\right)_{z^*=0}, \tag{15}$$

in which x_S is the specified mole fraction of the nutrient at the source. Analogously, the boundary conditions at the crystal interface are

$$T^*(r^*,1) = T_C^* \tag{16}$$

$$w(r^*,1) = \frac{N_M x_C}{1+(N_M-1)x_C} \tag{17}$$

$$v^*(r^*,1) = 0 \tag{18}$$

$$u^*(r^*,1) = -\frac{1}{1-w}\left(\frac{\partial w}{\partial z^*} + \frac{\alpha_T w}{T^*}\frac{\partial T^*}{\partial z^*}\right)_{z^*=1}, \tag{19}$$

where $T_C^* = T_C/T_S$.

The temperature distribution on the wall plays a key role in the magnitude and resulting effects of thermal creep. To provide a degree of freedom in choosing the temperature distribution – yet maintain a relatively simple form – we model the wall temperature in a piecewise–linear fashion. The distribution is described by two characteristic lengths; z_{hot} and z_{cold}. For wall positions between $z = 0$ and z_{hot} the wall temperature is equal to the source temperature, between z_{hot} and z_{cold} the wall temperature varies linearly from the source to the crystal temperature, and from $z = z_{cold}$ to L the wall temperature is equal to the crystal temperature. This distribution is somewhat representative of the three–zone arrangement employed in the NASA μg crystal growth furnace [15]. We also assume that deposition of the nutrient does not occur on the side wall. The boundary conditions on the side wall can then be stated in nondimensional form as

$$T^*(R^*,z^*) = \begin{cases} 1, & 0 \le z^* \le z^*_{hot} \\ 1-(1-T_C^*)\dfrac{z^*-z^*_{hot}}{z^*_{cold}-z^*_{hot}}, & z^*_{hot} < z^* < z^*_{cold} \\ T_C^*, & z^*_{cold} \le z^* \le 1 \end{cases} \tag{20}$$

$$\left.\frac{\partial w}{\partial r^*}\right|_{r^*=R^*} = 0 \tag{21}$$

$$u^*(R^*,z^*) = \left.\frac{C_s Sc}{\rho^* T^*}\frac{\partial T^*}{\partial z^*}\right|_{r^*=R^*} \tag{22}$$

$$v^*(R^*,z^*) = 0, \tag{23}$$

in which $R^* = R/L$. At the centerline of the ampoule we impose the usual symmetry conditions, which correspond to zero v^* and zero radial gradients of u^*, T^*, and w.

Solution of Eqs. (3–7) was accomplished using the SIMPLE algorithm as described by Patankar [16]. Discretization of the domain followed the staggered–grid procedure required by the SIMPLE method. A non–uniform grid was employed which concentrated grid points near the interfaces and walls of the ampoule. Typically, 23 grid points were used in the

radial direction, and up to 53 grid points were used in the axial direction. In all cases, the presented results for dimensionless velocities are within 0.5% of the values obtained when the number of grid points was doubled. Details of the solution method are given in Ref. [17].

3. Results and Discussion

3.1. System parameters

The relevant dimensionless parameters include those pertaining to the fixed boundary conditions (x_S, x_C, T_C^*, z_{hot}^* and z_{cold}^*), those describing the thermophysical and transport properties of the mixture (Sc, Pr, C_s, α_T and N_M), and those describing the ampoule geometry and environment (R^* and g^*). The actual value of the pressure number N_P is irrelevant (providing it is a positive number) since we assume pressure gradients have no effect on density.

Fixed values of parameters used in this work are $Pr = 1$, $C_s = 2.2$ (which represents the theoretical maximum), $z_{cold}^* = 1$, and $R^* = 1/5$. The Soret factor α_T is set either to zero (no thermal diffusion) or to $3Sc/4$ – which represents the limiting value attained for a dilute concentration of a high molecular weight nutrient in a low molecular weight carrier [14, 18].

It should be noted that, in principle, the ratio of nutrient mole fractions at the source and crystal interfaces could be related to the temperature ratio via a Clausius–Clapeyron equation for the specific crystal material and ampoule total pressure. We choose not to introduce such a relationship – since it would eliminate one parameter (e.g., x_C) by introducing another (the enthalpy of vaporization of the crystal). We treat the mole fractions and the temperatures as independent – yet attempt to assign values to them that are in the realm of physical plausibility.

3.2. Diffusive/thermal creep convective flows

We begin by examining the effect of thermal creep on the flowfield and interface flux in the absence of gravity and Soret diffusion. As a starting point, we consider a configuration that is somewhat representative of the H_2–I_2 system modelled in Refs. [5–8]. The molecular mass ratio is set to $N_M = 254/2 = 127$, and the source and crystal nutrient mole fractions are $x_S = 0.7$ and $x_C = 0.3$. The one–dimensional mass transfer Peclet number for this situation, which is defined [6]

$$Pe_{1D} = \frac{w_C}{x_C} \ln\left(\frac{1 - x_C}{1 - x_S}\right), \tag{24}$$

is 1.2. We take the dimensionless crystal temperature to be $T_C^* = 350/400 = 0.875$, which

represents a somewhat larger temperature difference across the ampoule than those used in the previous investigations.

We focus first on the effects of an increasing creep velocity throughout the entire ampoule. To do this, we impose a linear wall temperature distribution from the source to the crystal (i.e., $z^*_{hot} = 0$ and $z^*_{cold} = 1$) and vary Sc from 1 to 10 while holding all other parameters constant. This is, of course, somewhat inconsistent with physics – because an increasing Sc would generally be associated with an increasing N_M and a decreasing nutrient vapor concentration. Our rationale for this approach, however, is that the next level of approximation would require an accounting of the effects of mixture composition on transport properties. We wish to avoid over–specifying the system – and keep the model simple to the maximum extent possible. We also note that for the buoyancy–free and Soret–free systems, the dimensionless velocity results are not appreciably altered by the value of N_M.

Figure 2 shows the velocity field that results from the combined actions of the Stefan flow and thermal creep at the side wall, with $Sc = 1$ on the left plot and 10 on the right. The scale of the vector arrows is the same in both plots. Note first that the case with $Sc = 1$ results in a velocity field that is practically indistinguishable from the zero–slip case. This is not surprising, because the creep/Stefan velocity ratio, defined in Eq. (2), is $u_c/u_D \approx 0.2$ for this case. Upon increasing Sc to 10, the creep velocity at the wall becomes comparable to the Stefan velocity. The combined effect results in a recirculating flow, with the cold fluid pumped towards the source along the walls, and returning to the crystal along the ampoule centerline.

Even though thermal creep results in a roughly twofold increase in centerline velocity for $Sc = 10$, the total mass transfer rate to the crystal is only slightly increased (ca. 5%) by the creep–induced recirculation. The recirculating flow does, however, have a significant effect on the distribution of mass flux at the crystal interface. Shown in Fig. 3 are growth distributions as a function of radius for Sc ranging from 1 to 10, with all other model conditions the same as in the previous plot. We present a renormalized mass flux, which corresponds to the ratio of the dimensionless normal velocity at the interface divided by the 1–D Peclet number predicted from Eq. (24). For the $Sc = 1$ case the velocity distribution is essentially unchanged from that attained in the absence of creep. The fact that the distribution is not completely uniform in this case is due to the recirculation of the carrier in the ampoule, as discussed in Ref. [6]. An increasing magnitude of the creep velocity, brought on by large values of Sc, augments the radial segregation of the nutrient concentration above the interface. Centerline growth rates are seen to increase by roughly 20 percent for the given range of Sc, which are balanced by a decrease in growth at the edges of the interface.

A linearly decreasing wall temperature distribution thoughout the entire ampoule is not representative of actual PVT conditions. Frequently, the wall is maintained at a temperature at or above the source temperature to a position just above the crystal interface – the point being to prevent the parasitic nucleation of the nutrient onto the wall [8]. With regard to thermal creep, this effect would increase the temperature gradient – and resulting creep velocity – at the wall adjacent to the interface. To investigate this effect, we changed the location of z^*_{hot} to points progressively closer to the crystal while maintaining $Sc = 5$ and all other conditions the same as in the previous results. Plots of the velocity field for $z^*_{hot} = 0.75$ and 0.875 are given in Fig. 4. A vortex is now created within the ampoule section corresponding to the wall temperature gradient, which increases in intensity as the length of the section decreases. Normalized growth distributions calculated for the changing wall temperature distributions are plotted in Fig. 5, with the same normalization used in Fig. 3. As can be seen, a steepening of the wall gradient leads to an increasingly nonuniform growth distribution – with the greatest effects occuring at the edges of the interface. The central factor here is that the creep–induced recirculation occurs directly above the interface – and thus has a direct influence on the transport of nutrient at the crystal–vapor boundary. This behavior could be significantly reduced or eliminated by minimizing the wall temperature gradient at the interface.

3.3. Thermal creep and Soret diffusion

The results of the previous section indicate that creep flows will have bearing on vapor transport only for relatively large Sc and small T^*_C. Large Sc values are typically associated with a large nutrient/carrier molecular mass ratio and a vanishingly small mass concentration of the nutrient in the gas – which will yield the maximum values of the Soret factor α_T. The 'creep regime' would thus be synonymous with a significant Soret transport of the vapor. This equivalence is not surprizing. Soret diffusion can be viewed as a molecular thermophoresis – especially in the limit of large nutrient molecules [14]. Thermal creep at the wall and Soret transport of the vapor originate from the same fundamental mechanism – i.e., temperature gradients – and conditions which are favorable to one will be favorable to the other.

To model such conditions, we chose dimensionless parameters that were representative of the copper phthalocyanine PVT experiments conducted by Debe et al. [3]. Specifically, we used $T^*_C = 360/600 = 0.6$, $x_S = 10^{-3}$, $x_C = 10^{-5}$, $N_M = 600/30 = 20$, $Sc = 10$ and $g^* = 0$. The one–dimensional Peclet number for this condition is $Pe_{1D} \approx 0.02$ Information on the wall temperature distribution is not obtainable from Ref. [3]; we therefore considered separate cases in which the location of z^*_{hot} was moved from the source to the crystal.

Similar to thermal creep, the effect of Soret diffusion on nutrient transport to the

crystal is strongly dependent on the thermal boundary conditions of the side wall. Unlike mass transfer, heat is transferred to (and, occasionally, from) the ampoule through the side walls. The temperature distribution in the gas – and its resulting effect on the concentration distribution via Soret diffusion – can therefore be highly two dimensional. To illustrate this behavior, we show in Fig. 6 contour plots of the nutrient mass fraction w in the ampoule, calculated without thermal creep, for different locations of z^*_{hot}. For the low–Pe conditions used here, the linear temperature distribution ($z^*_{hot} = 0$) is closely representative of an adiabatic wall. Heat transfer for this case is essentially one–dimensional, and acts to transport the nutrient uniformly to the crystal. Note also that the mass fraction field for the $z^*_{hot} = 0$ case is qualitatively similar to that attained under high Pe, convective/diffusive conditions – in that the nutrient tends to 'pile up' at the crystal interface. Indeed, the processes of convection (via the Stefan flow) and Soret transport of nutrient are analogous for the given conditions. Within the bulk gas nutrient transport is dominated by Soret diffusion. At the crystal, however, the contribution of Soret diffusion essentially vanishes (because of the relatively small mass fraction of nutrient at the crystal), and deposition becomes controlled by Fickian diffusion.

As z^*_{hot} is moved away from the source and towards the crystal, a progressively larger fraction of the heat that is transferred to the crystal originates from the heated side walls of the ampoule. This creates a two–stage effect within the mass fraction field. For regions well within the heated wall zone the temperature is nearly uniform at T_S. Nutrient transport therefore becomes controlled within this zone by the relatively slow process of Fickian diffusion – which results in the high concentration gradients. At the transition point between the heated and gradient zones, radial heat transfer from the wall acts to drive the nutrient towards the centerline. At the same time, the large axial temperature gradients within the gradient zone accelerate the transport of nutrient, which results in the low concentration gradient within this second zone.

The radial segregation of the nutrient that results from wall heat transfer can, as expected, have a significant effect on the flux distribution at the interface. This is demonstrated in Fig. 7, in which we plot the normalized interface velocities for different z^*_{hot} locations. Similar to the thermal creep effects discussed in Sec. 3.2., moving z^*_{hot} closer to the interface results in progressively nonuniform, axial–peaked growth distributions. The extreme (and idealized) case of $z^*_{hot} = 1$ (i.e., a wall entirely at the source temperature) results in a complete absence of deposition for interface positions adjacent to the wall. This particular case actually resulted in physically–impossible results in the wall–interface corner (e.g., negative values of w) – which are a numerical artifact of the essentially infinite temperature gradient at the corner. The effect of Soret diffusion on the total mass transfer rate, on the other hand, is greatest for $z^*_{hot} = 0$ (i.e., an adiabatic wall) – since this

condition results in an axial temperature gradient across the entire length of the ampoule.

For the given model conditions, the thermal creep velocity is on the order of 500 times greater than the characteristic diffusion velocity. Consequently, including creep into the model results in convectively–dominated mass transport within the gradient section of the ampoule – as opposed to essentially convection–free conditions in the absence of creep. The recirculation generated by the creep has a controlling role on the distribution of flux at the interface, and the interfacial velocity profiles (shown in Fig. 8) attain a form that is qualitatively similar to those shown in Fig. 5. Soret diffusion, on the other hand, now affects primarily the overall mass transport to the interface. As was the case in the results of Sec. 3.2., inclusion of thermal creep has a relatively small effect on the total transfer of the nutrient.

3.4. Effect of creep on buoyant convection

The large Sc and large ΔT conditions in which creep becomes significant would correspond to conditions in which gas density is controlled primarily by temperature. It is therefore relevant to compare creep to buoyant flows that are driven by thermal expansion – as opposed to solutal–driven convection. To examine the interplay between buoyancy and creep, we performed calculations using the same conditions as in the previous section, except with $T_C^* = 0.8$ and $z_{hot}^* = 0.75$, and varied g^* from 0 to -5×10^7. The negative value of g^* indicates source–directed gravity, which represents the unstable configuration (for thermal expansion) of the crystal on top. As a point of reference, an ampoule of 10 cm length, with $D_{AB} = 12.4$ cm^2/s (which corresponds to the CuPc value used in Ref. [3] at 5.4 torr total pressure) would have $g^* = -6.3 \times 10^3$. Since D_{AB} varies inversely proportional to total pressure, the chosen range of $g*$ would represent operation of this experiment at total pressures up to about 0.6 atm.

Before presenting results of our calculations, we should note that the axisymmetric formulation of our model is of questionable validity for buoyant convection in vertical cylinders [7]. However, in the absence of thermal creep, the heated side walls of the ampoule would be expected to stabilize an initial axisymmetric buoyant recirculation as g^* decreases from zero. The gas, heated by the walls, would rise along the walls to the crystal and sink towards the source along the centerline. We have confirmed this behavior in limited calculations using a 2–D, cartesian representation of the ampoule (similar to that used in Ref. [8]), with equivalent interface and side wall boundary conditions. Once $-g^*$ exceeds a critical value the axisymmetric roll would become unstable, and would transform to a single, asymmetric roll. Based upon our 2–D cartesian model, the transformation to a single roll occurs for $g^* \approx -2 \times 10^7$ for the given model conditions. Since a cylindrical system would be expected to be more stabilizing than a 2–D cartesian system, the axisymmetric

assumption is probably valid throughout the given range of g^*. Of course, validation of this assumption would require a 3–D model – which is beyond our current computational capabilities.

A distinguishing feature between creep recirculation and expansive buoyant recirculation is that they occur in opposite directions. Creep drives the gas along the gradient section of the wall towards the source, whereas buoyancy is directed along the wall towards the crystal. The creep flow would thus be expected to inhibit the development of buoyant recirculation for this particular configuration. The interaction between creep and buoyant flows is graphically illustrated in Fig. 9, in which we present velocity vectors calculated for $g^* = -5 \times 10^5$ (left), -5×10^6 (middle), and -2×10^7 (right). The scale of the velocity vector is the same in all plots. At the smallest value of g^* the recirculation is completely dominated by the creep flow. At the next g^* level creep still controls the convection within the gradient zone, yet buoyancy is seen to have created a counter–rotating vortex directly below the creep–produced recirculation. Finally, increasing g^* to -2×10^7 results in an extremely complicated flow pattern. The upwards, buoyancy–controlled flow now extends to the crystal, and the creep–generated vortex has been pushed into a thin region adjacent to the side wall.

The transition from creep to buoyancy controlled convection is reflected in the interfacial velocity profiles, which are shown in Fig. 10 for the same conditions as in Fig. 9. Also shown are profiles calculated in the absence of thermal creep. The effect of combined creep and buoyant flows is seen to be qualitatively similar to that obtained by superimposing the separate velocity profiles for pure creep and pure buoyant convection. This behavior is somewhat expected. Even though the creep flow has a major effect on nutrient transport, the transport of energy and momentum are still controlled primarily by diffusion – for which a superposition of the independent creep and buoyant and flow fields becomes appropriate. This is further illustrated by examination of the total mass transfer rate to the crystal, denoted as j^*, as a function of g^*. We present this information in Fig. 11 for the zero–slip and thermal creep predictions, in which j^* has been normalized by $j^*_{1D} = \pi R^{*2} Pe_{1D}$. Thermal creep is seen to slightly delay the onset of buoyant convection control of mass transfer – which is indicated by the sudden increase in j^* near $g^* \approx -2 \times 10^7$ – yet for the most part the trends with and without thermal creep are similar.

Calculations were also performed, using the same conditions, of creep in conjunction with buoyancy stabilized (crystal on bottom) conditions. The results for this case show that the effects of creep are not appreciable altered by the presence of stabilized gravity relative to that calculated for zero gravity.

4. Summary

The results of this investigation reveal that, for certain operating conditions, thermal creep at the ampoule side walls can significantly re–distribute the mass flux arriving on PVT crystal interfaces. In general, the investigation supports the conclusions drawn from the order–of–magnitude estimates of Refs. [12, 13], in that the effects of creep become most evident for relatively large Sc, large ΔT and small Pe conditions. Indeed, flows resulting from normal–gravity buoyant convection can become, in this regime, relatively minor compared to the often–assumed 'higher–order' mechanism of thermal creep.

The model we have presented, however, is highly idealized, and is not meant to be a precise prediction of growth processes in actual PVT experiments. The crystal interfaces in such experiments will not be isothermal because of latent heat release by the depositing vapor and finite conduction heat transfer resistance in the crystal [17, 19]. The interfaces will also not remain planar – especially in the presence of mechanisms (such as buoyancy, thermal creep and Soret diffusion) that tend to nonuniformly distribute the flux at the interface. Another uncertainty in the present analysis are the values of the slip coefficient on the side walls (C_s) and the Soret coefficient (α_T). Our model predictions used the theoretical maximum values of these properties, and consequently the actual effects of thermal creep and Soret diffusion will likely be smaller than those predicted here. Nevertheless, our results strongly indicate that these frequently–disregarded mechanisms can have bearing on vapor transport – and should therefore be considered in detailed, comprehensive modelling efforts of actual PVT processes.

Acknowledgements

This project has been supported by NASA–MSAD through grant NAG8–977, Benjamin Penn, Contract Administrator. The authors have benefited from helpful discussions with Daniel Rosner.

References

[1] F. Rosenberger, Fundamentals of Crystal Growth, (Springer, N.Y., 1979).

[2] H. Wiedemeier and D. Chandra, J. Crystal Growth 57 (1982) 159.

[3] M. K. Debe, R. J. Poirier, E. L. Cook, L. R. Miller, M. S. Spiering, and S. P. Floeder, J. Vac. Sci. Tech. A 8 (1990) 49.

[4] L. van den Berg and W. F. Schnepple, Nucl. Instr. Methods A 283 (1989) 335.

[5] B. L. Markham and F. Rosenberger, Chem. Eng. Comm. 5 (1980) 287.

[6] D. W. Greenwell, B. L. Markham, and F. Rosenberger, J. Crystal Growth 51 (1980) 413.

[7] B. L. Markham, D. W. Greenwell, and F. Rosenberger, J. Crystal Growth 51 (1980) 426.

[8] A. Nadarajah, F. Rosenberger, and J. I. D. Alexander, J. Crystal Growth 118 (1992) 49.
[9] D. E. Rosner, Phys. Fluids A1 (1989) 1761.
[10] L. Talbot, R. K. Cheng, R. W. Schefer, and D. R. Willis, J. Fluid Mech. 101 (1980) 737.
[11] E. H. Kennard, Kinetic Theory of Gases, (McGraw–Hill, N.Y., 1938), p. 327-330.
[12] L. G. Napolitano, A. Viviani, and R. Savino, Acta Astronautica 28 (1992) 197.
[13] A. Viviani, and R. Savino, J. Crystal Growth 133 (1993) 217.
[14] J. L. Castillo, P. L. Garcia, and D. E. Rosner, J. Crystal Growth 116 (1991) 105.
[15] Teledyne Brown Engineering, Document SP–DOC–6102, (1990).
[16] S. V. Patankar, Numerical Heat Transfer and Fluid Flow, McGraw-Hill, N.Y., 1980.
[17] D. W. Mackowski, V. R. Rao, and R. W. Knight, J. Crystal Growth, submitted for publication (1996).
[18] E. A. Mason, J. Chem. Phys 27 (1957) 782.
[19] J. R. Abernathy, D. W. Greenwell, and F. Rosenberger, J. Crystal Growth 47 (1979) 145.

Figure Captions

1. Ampoule Schematic
2. Dimensionless velocity vectors for $Sc = 1$ (left) and $Sc = 10$ (right), for a linear temperature gradient across entire ampoule side wall. Other model parameters described in text. Origin of domain is lower left corner.
3. Normalized interfacial velocities vs. dimensionless radial position r/R as a function of Sc, other conditions the same as in Fig. 2.
4. Dimensionless velocity vectors for $z^*_{hot} = 0.75$ (left) and $z^*_{hot} = 0.875$ (right), with $Sc = 5$ and all other parameters the same as in Fig. 2.
5. Normalized interfacial velocities vs. dimensionless radial position as a function of z^*_{hot}, other conditions the same as in Fig. 2.
6. Constant–value contours of nutrient mass fraction for $z^*_{hot} = 0$ (left), $z^*_{hot} = 0.5$ (middle), and $z^*_{hot} = 0.875$ (right). Zero slip boundary condtions, diffusive and Soret transport of nutrient.
7. Normalized interfacial velocities vs. dimensionless radial position as a function of z^*_{hot} for the conditions of Fig. 6.
8. Normalized interfacial velocities vs. dimensionless radial position for the conditions of Fig. 7, with the addition of thermal creep convection.
9. Dimensionless velocity vectors for $g^* = -5\times10^5$ (left), -5×10^6 (middle), and -2×10^7 (right).
10. Normalized interfacial velocities vs. dimensionless radial position as a function of g^*, for thermal creep and zero slip conditions.
11. Normalized total mass transfer rate vs. g^* for thermal creep and zero slip conditions.

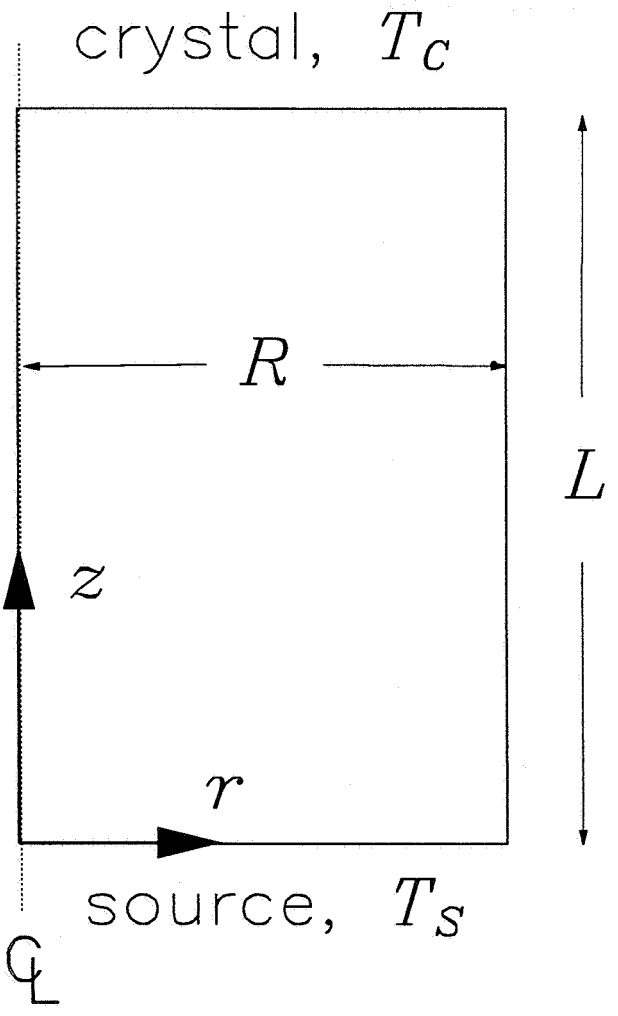

Fig. 1, Mackowski et al.

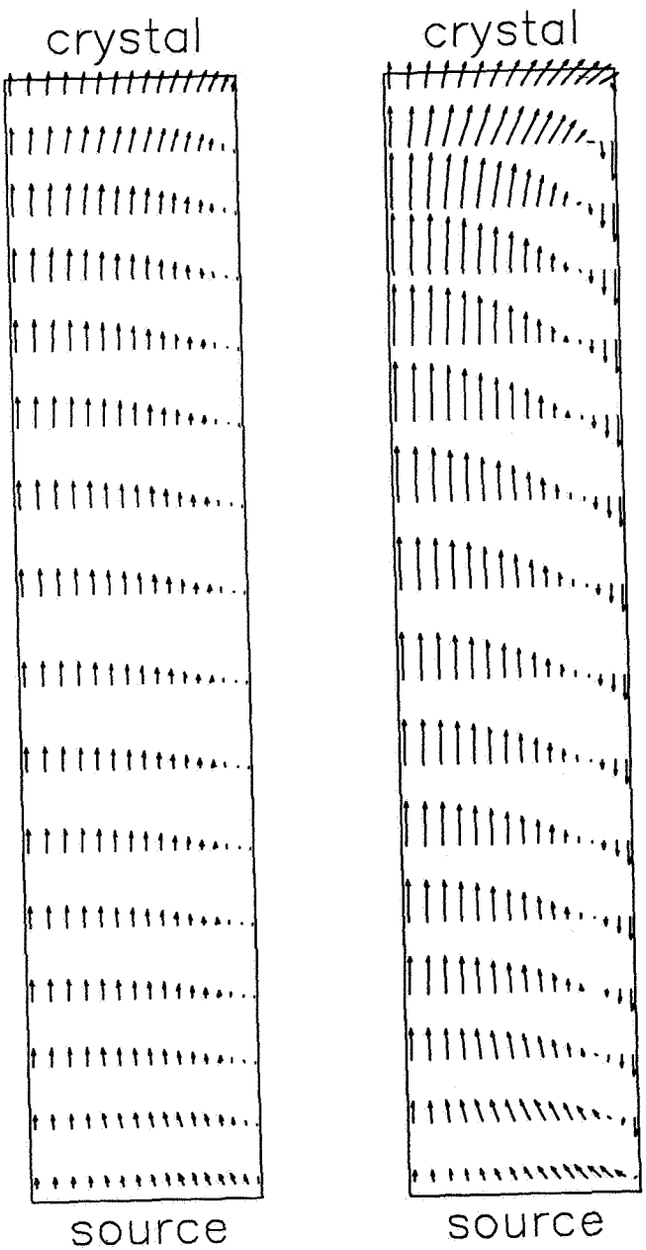

Fig. 2, Mackowski et al.

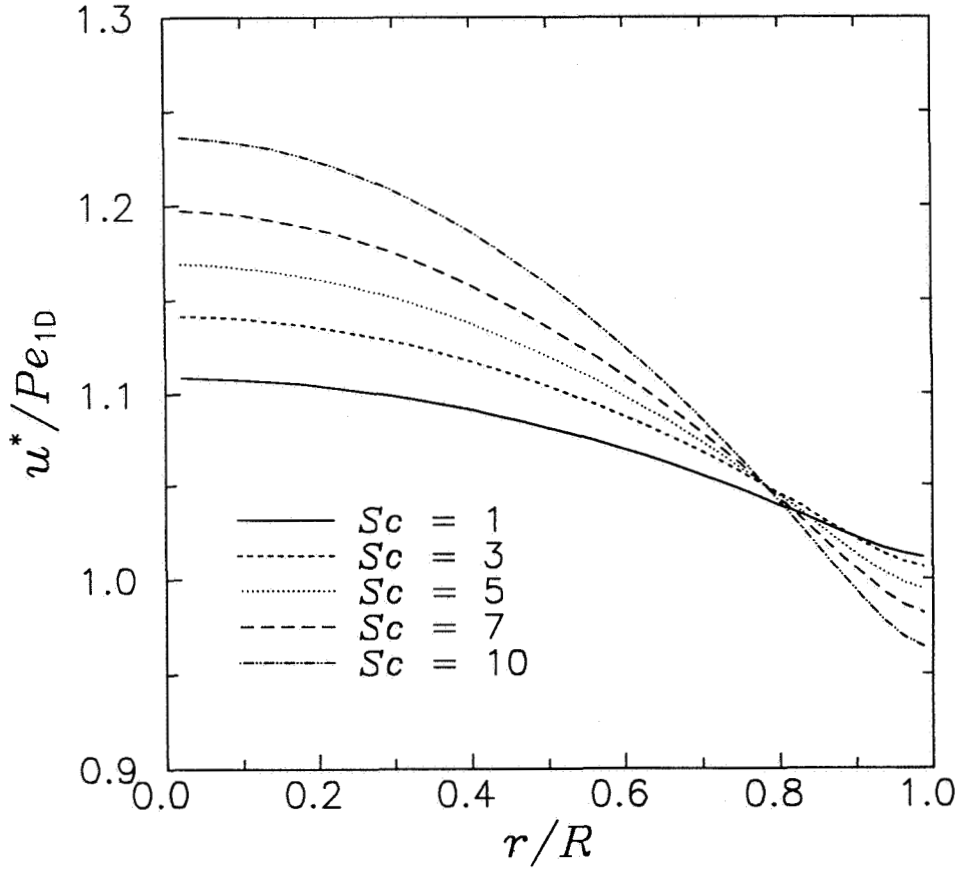

Fig. 3, Mackowski et al.

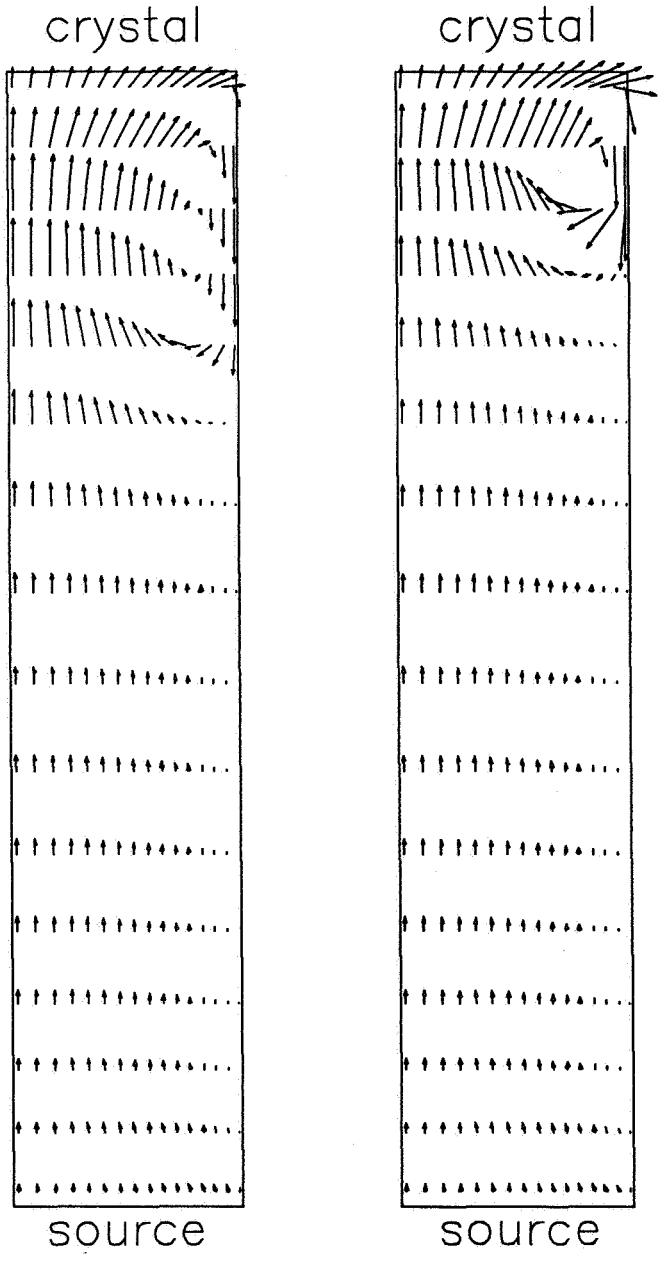

Fig. 4, Mackowski et al.

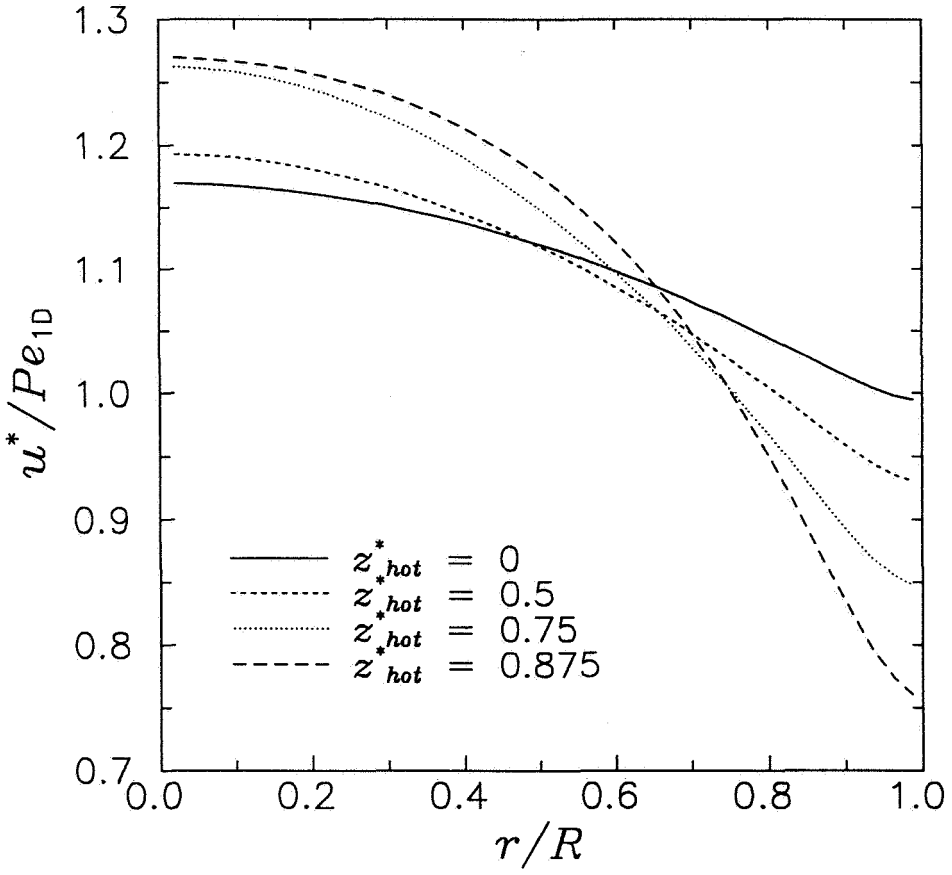

Fig. 5, Mackowski et al.

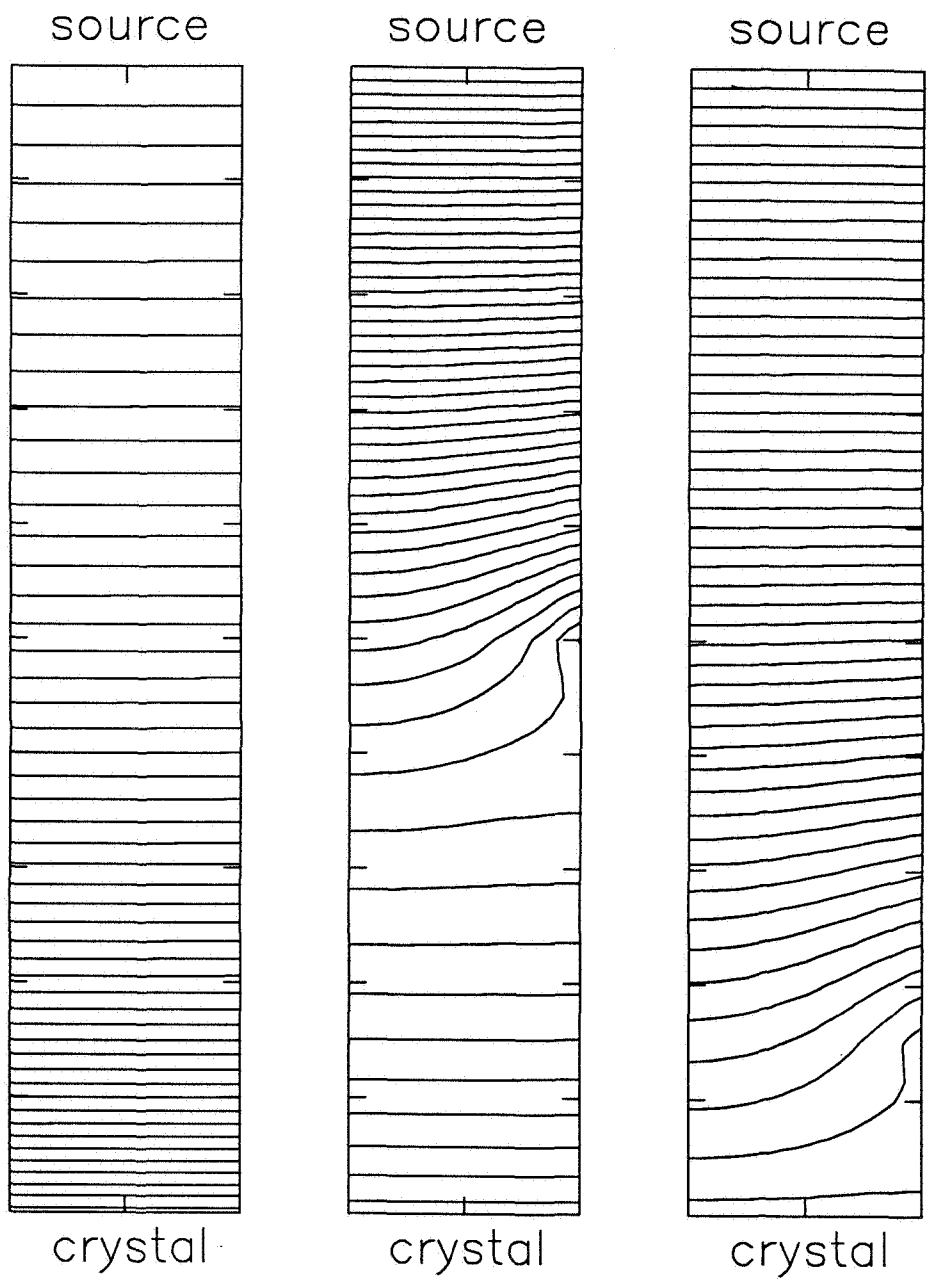

Fig. 6, Mackowski et al.

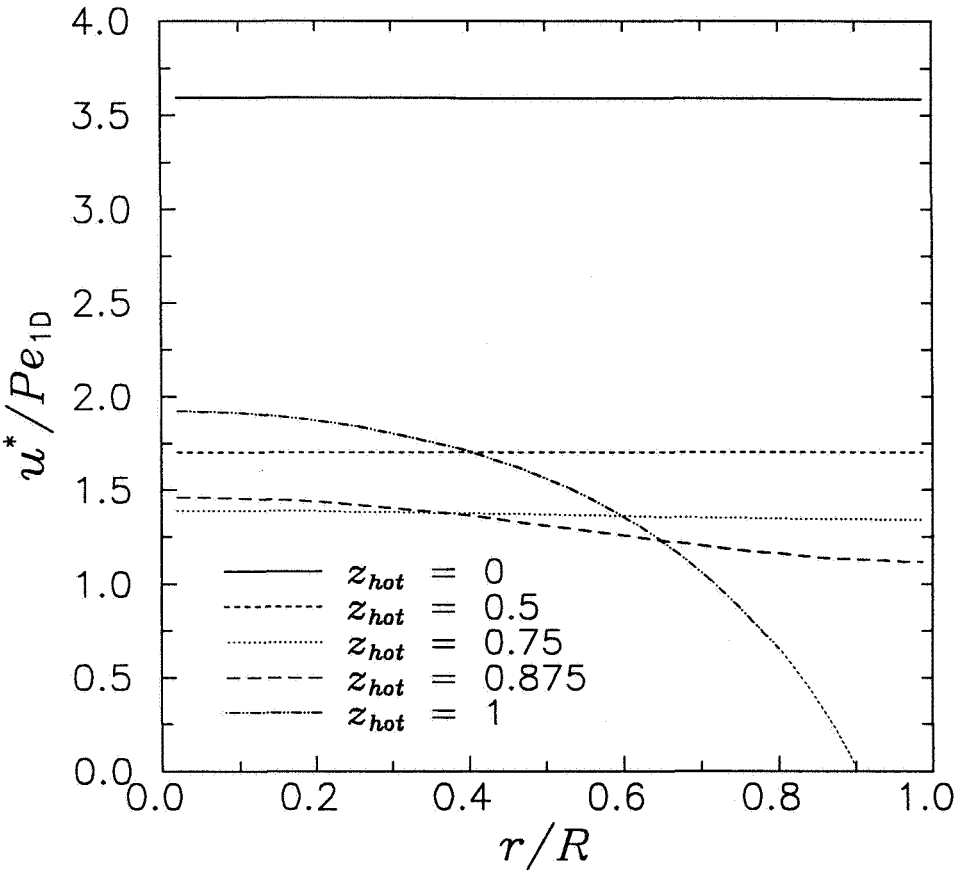

Fig. 7, Mackowski et al.

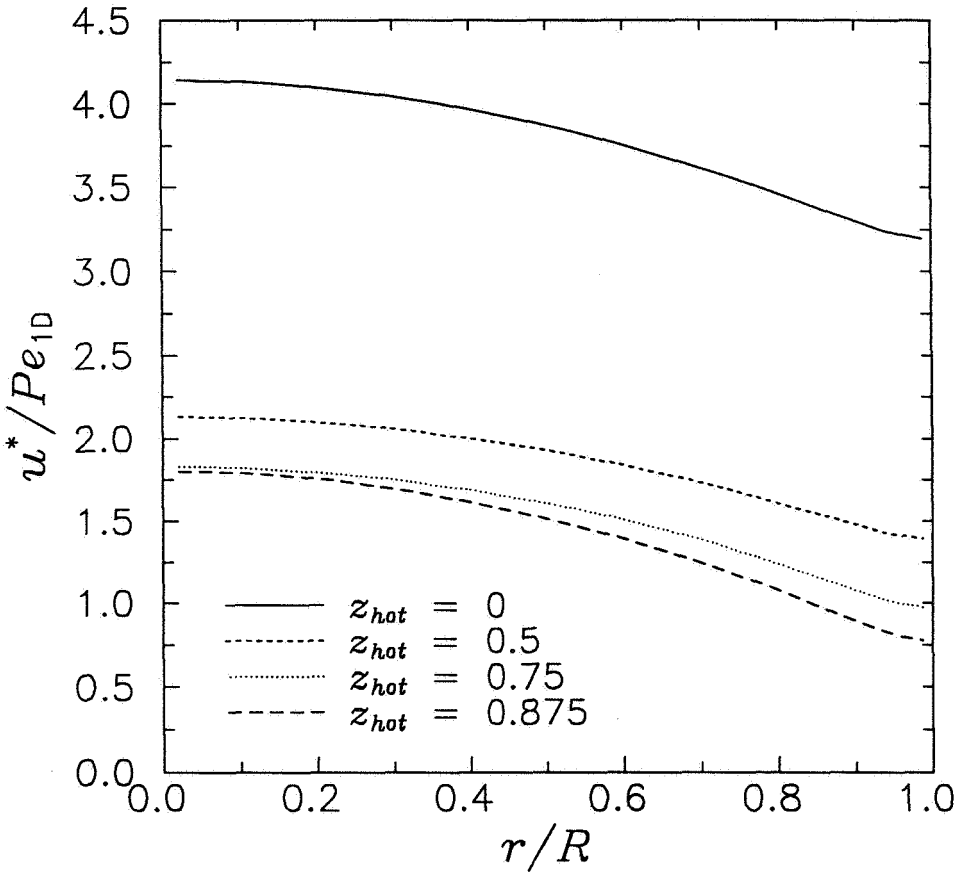

Fig. 8, Mackowski et al.

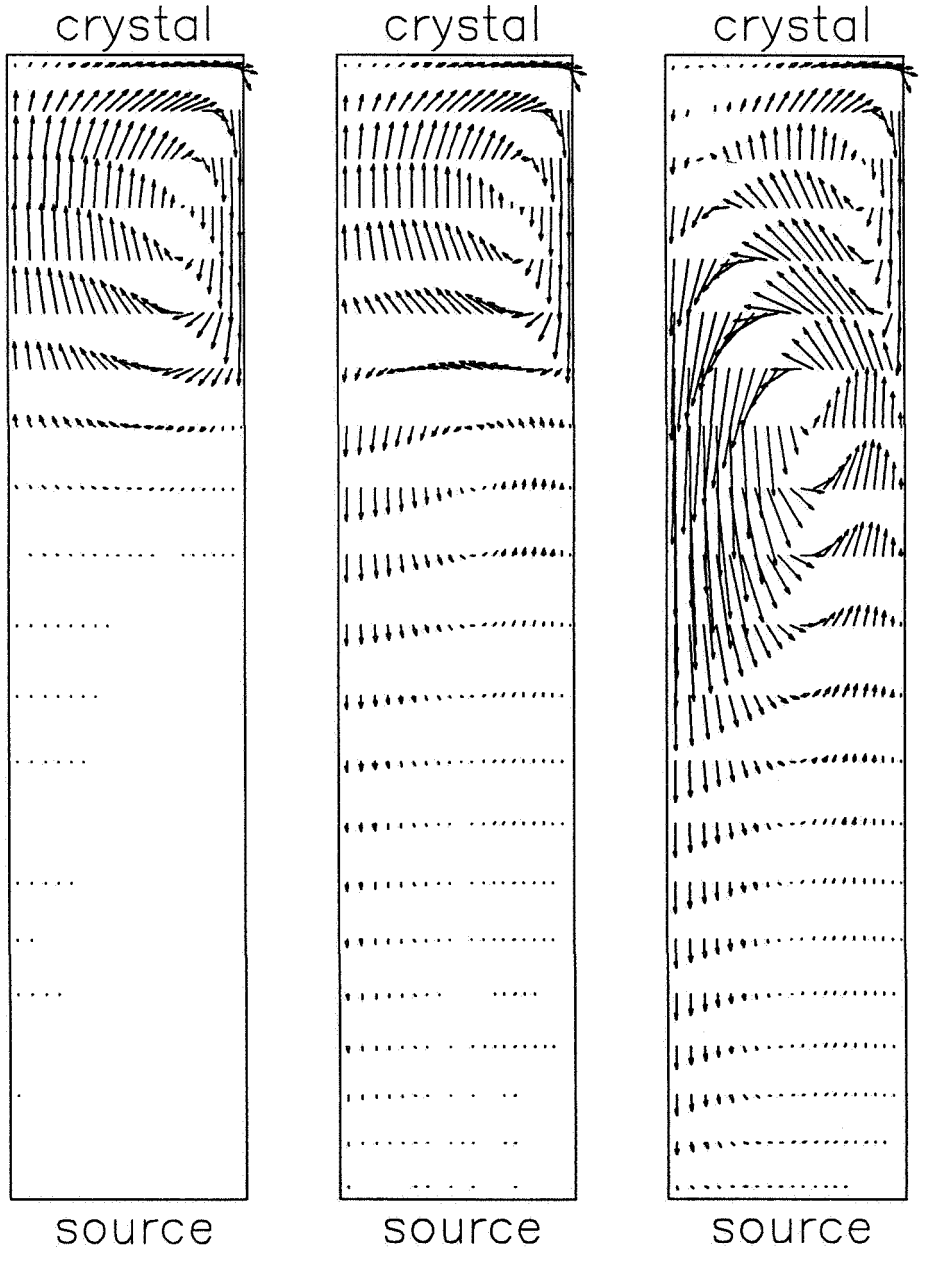

Fig. 9, Mackowski et al.

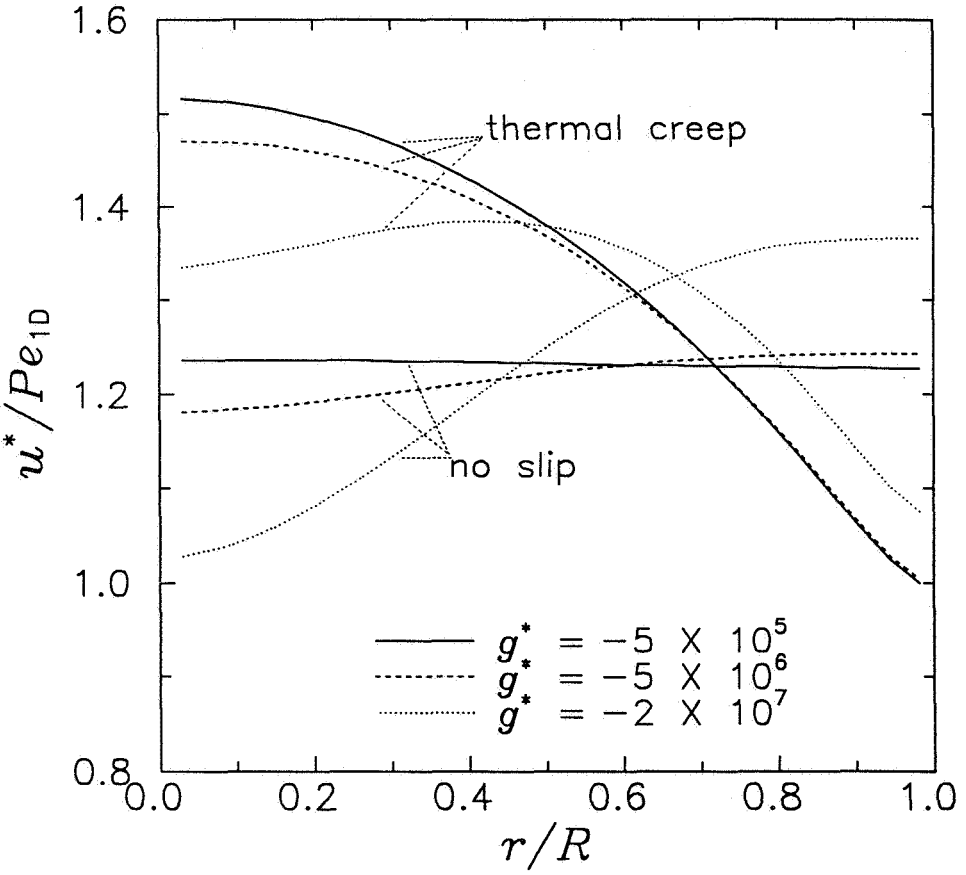

Fig. 10, Mackowski et al.

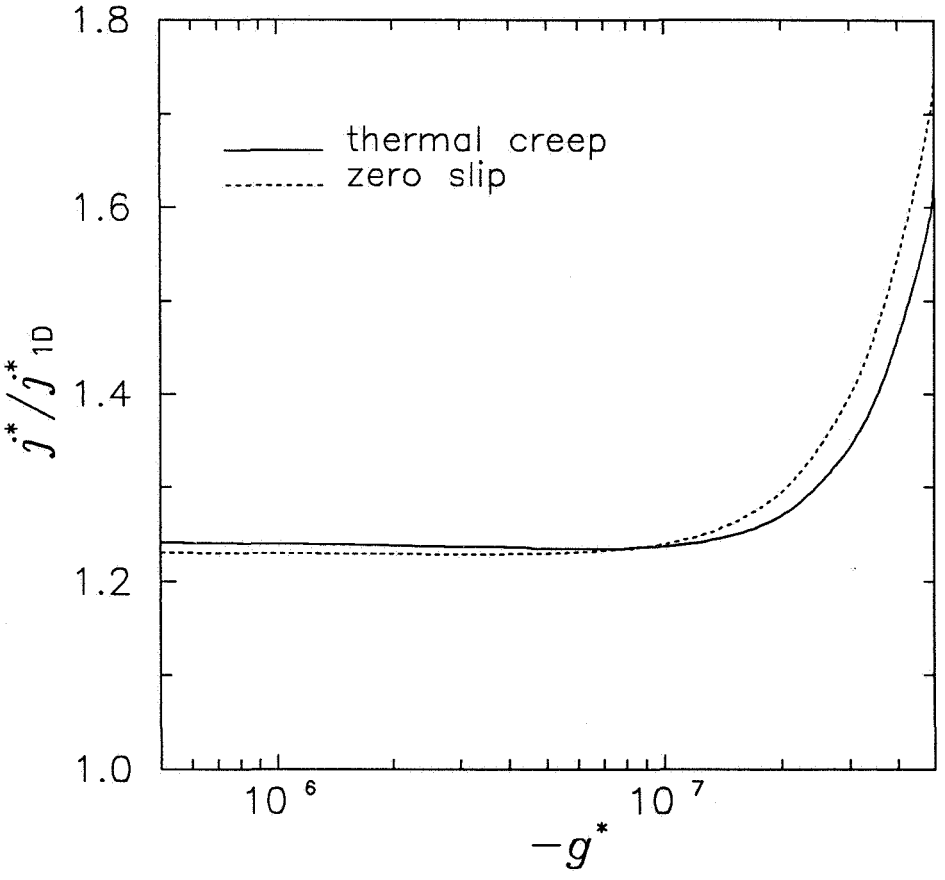

Fig. 11, Mackowski et al.

Appendix B

Effect of Solid Phase Heat Transfer and Wall Deposition on Crystal Growth in Physical Vapor Transport Ampoules

Daniel W. Mackowski, Rammohan Rao, and Roy W. Knight

Mechanical Engineering Department
Auburn University, AL 36849, USA

To appear, *J. Crystal Growth*, 1996

Abstract

A numerical investigation of binary component, convective/diffusive physical vapor transport in cylindrical ampoules is presented. We specifically examine the effects of 1) conduction heat transfer within the crystal, and 2) deposition of the vapor onto the ampoule side walls, on the growth rates and growth uniformity of the crystal. A two–dimensional numerical model of heat and mass transfer within the crystal and vapor regions of the ampoule is developed. Calculations are performed for H_2–I_2 transport systems in unit and zero gravity conditions. Results indicate that the latent heat release from the depositing vapor can significantly affect the interface temperature distribution of finite–thickness crystals. Depending on the thermal boundary conditions at the crystal side walls, heat transfer within the crystal can either increase or decrease the uniformity of mass flux at the interface. The predicted transport conditions under which heat transfer has a controlling role on crystal growth are consistent with a simplified, one–dimensional analysis of combined heat and mass transfer in PVT ampoules. Calculation results also reveal that deposition of the vapor onto the side walls of the ampoule can lead to highly nonuniform distributions of mass flux at the crystal interface. Furthermore, side wall deposition can result in buoyant recirculation even when the ampoule is oriented in a convectively stable configuration. This phenomenon can result in interface flux distributions that are considerably different than those obtained under zero gravity environments for the same model conditions.

1. Introduction

In the most general sense, crystal growth by physical vapor transport (PVT) involves the steps of 1) sublimation of a nutrient vapor from an amorphous source 2) transport of the vapor through an inert carrier gas to a substrate that is maintained at a lower temperature than the source, and 3) deposition of the vapor onto the substrate forming a crystal. As noted by Rosenberger [1], the quality of crystals that are grown in this process are governed largely by the heat and mass transfer mechanisms that occur within the PVT ampoule. Since the density of the gas can vary significantly within the ampoule, buoyancy–driven convection can often become a dominant mode of vapor transport. Numerical investigations by Markham et al. [2], and more recently Nadarajah et al. [3], have quantified the effects of buoyant convection on the flux distribution in PVT ampoules. As expected, buoyant recirculation of the vapor within the ampoule can lead to highly nonuniform distributions of mass flux at the crystal surface.

To reduce this effect while maintaining relatively high transport rates, the potential of manufacturing crytals under microgravity (μg) conditions has received a fair amount of attention. Indeed, crystals grown in μg PVT experiments have been shown to posess uniquely different and improved structural properties than those grown on earth [4–6]. At this time, however, it is not certain whether the differences result from modified vapor–phase transport conditions, or are due to the elimination of weight stress in the crystals. The combined numerical investigations of Greenwell et al. [7] and Markham et al. [2] would indicate that vapor transport under convectively–stabilized, unit gravity conditions (i.e., when the high–density vapor is on the bottom) is not markedly different than zero–gravity conditions.

The numerical investigations in Refs. [2, 3, 7], however, were limited to conditions of an isothermal crystal interface and zero deposition on the side walls of the ampoule. As noted in Ref. [3], an isothermal interface would not be realistic for poorly conducting crystals. Latent heat release of the depositing vapor can result in a large heat flux at the interface, and the interface temperature distribution would be dependent on the distribution of the heat flux as well as the removal of heat from the crystal. Since the saturation vapor pressure of the nutrient is often highly sensitive to temperature, a relatively small variation in temperature across the crystal surface could have an appreciable effect on the local growth rates. It has been observed that conduction of heat from the crystal to the side walls of the ampoule can lead to a preferential deposition of vapor at the wall, ultimately resulting in a concave interface shape [8].

The purpose of this paper is to examine the roles of heat conduction in the crystal and deposition onto the side walls on the growth process in convective/diffusive PVT systems. We begin by presenting a one dimensional analysis of combined heat and mass transfer in

PVT ampoules, which will provide a simple estimate of the conditions at which growth becomes controlled by heat conduction in the crystal. Next, we use a two–dimensional numerical model to predict the effects of crystal conduction and wall deposition on the mass flux distribution for unit and zero gravity environments.

2. Model

2.1. One dimensional heat/mass transfer

An analysis of pure mass transfer in one–dimensional, steady state PVT systems has been presented in Ref. [7]. More recently, Louchev and Zaletin [9] developed a one–dimensional model for combined solid phase heat transfer and gas phase mass transfer in small Peclet number regimes (i.e., dominant diffusive transfer of the vapor). Here, we extend the one–dimensional model to include convective/diffusive heat and mass transport.

The geometry of the PVT ampoule is schematically illustrated in Fig. 1. The ampoule is cylindrical, with length L and radius R. Nutrient vapor, denoted as species A, originates from the source at $z = 0$ and deposits onto the crystal at $z = L$. A constant mass of carrier gas resides within the ampoule, denoted as species B. The thickness of the crystal is δ. Temperature and mole fraction are assumed to vary only in the z–direction, and all other properties are constant. We assume that the translation rate of the crystal interface is significantly smaller than the mass–averaged velocity of the vapor (which is appropriate for the highly disparate densities of the solid and gas) so that the system can be considered to be in steady state at any instant. The temperature of the source is T_S, and the ending wall is maintained at $T_{C,0}$.

Unlike the model of Louchev and Zaletin [9], we restrict our analysis to infinite–rate deposition kinetics at the source and crystal interfaces. The nutrient vapor partial pressure at the interfaces will then be given by the equilibrium values at the interface temperatures. We also neglect radiation heat transfer within the ampoule. These restrictions will be appropriate for the carrier partial pressures ($\sim$ 100 torr), operating temperatures ($\sim$ 370 K), and crystal materials (iodine) that are the subject of this investigation.

The mass transfer Peclet number will be given by [7]

$$Pe = \frac{u^* L}{D_{AB}} = \ln\left(\frac{1 - x_{A,i}}{1 - x_{A,S}}\right), \tag{1}$$

where u^* is the mole–averaged velocity, D_{AB} is the binary diffusion coefficient, x_A is the mole fraction of the nutrient, and subscript i denotes the value at the crystal interface. The mole fraction at the interface can be related to the interface temperature $T_{C,i}$ by evaluation of the Clausius Clayperon equation between $T_{C,i}$ and T_S;

$$\ln\left(\frac{x_{A,i}}{x_{A,S}}\right) = \frac{h^*_{sg}}{R_u T_S}\left(1 - \frac{T_S}{T_{C,i}}\right), \tag{2}$$

in which h^*_{sg} is the molar latent heat of sublimation for species A and R_u is the universal gas constant. Combining the two previous equations results in an expression for Pe in terms of nondimensional thermal and thermodynamic properties of the system;

$$Pe = \ln\left(\frac{1 - x_{A,S}\exp\left[-H\theta_i/(1-\theta_i)\right]}{1 - x_{A,S}}\right), \tag{3}$$

in which $H \equiv h^*_{sg}/R_u T_S$ and $\theta_i \equiv 1 - T_{C,i}/T_S$.

The crystal interface temperature will depend on the dynamics of heat transfer through both the gas and the crystal. The gas and solid phase conductive fluxes at the crystal interface are related by

$$q''_s - q''_g = Cu^*\overline{h}_{sg}. \tag{4}$$

The temperature distribution in the solid can be taken to be linear (1–D conduction), for which $q''_s = k_s(T_{C,i} - T_{C,0})/\delta$. The gas phase conductive flux can be obtained from a one–dimensional analysis of diffusive/convective heat transfer in the ampoule, which yields

$$q''_g = \frac{k_g(T_S - T_{C,i})}{L} \cdot \frac{Pe\,Le}{1 - \exp(-Pe\,Le)}, \tag{5}$$

where $Le = k_g/Cc^*_pD_{AB}$ is the Lewis number, and C, k_g and c^*_p are the molar concentration, thermal conductivity and molar specific heat, of the gas. With these substitutions, the nondimensional form of Eq. (4) becomes

$$\left(\phi + \frac{Pe\,Le}{1 - \exp\left(-Pe\,Le\right)}\right)\theta_i = \phi\theta_C - Pe\,Le\,H\,(1 - \frac{1}{\gamma}). \tag{6}$$

In the above, $\phi \equiv (k_s/\delta)/(k_g/L)$ is the ratio of gas and solid conduction heat transfer resistances, $\theta_0 \equiv 1 - T_{C,0}/T_S$, and γ is the ratio of specific heats of the gas. Taken together, Eqs. (3) and (6) form a nonlinear relation for the Peclet number as a function of the nondimensional parameters ϕ, θ_0, H, Le, γ, and $x_{A,S}$. The mole fraction of A at the source can be eliminated using the Peclet number for $T_{C,i} = T_{C,0}$ (i.e., zero crystal thickness), denoted as Pe_0, via

$$x_{A,S} = \frac{1 - \exp\left(-Pe_0\right)}{1 - \exp\left[-H\theta_0/(1-\theta_0) - Pe_0\right]} \tag{7}$$

As ϕ decreases, the mass transfer process will become limited by conduction heat transfer in the solid. In the limit of $\phi \to 0$ (for which $\theta_i \to 0$ and $Pe \ll 1$), Eq. (6) predicts that $Pe \propto \phi$, i.e., mass transfer will be proportional to k_s and inversely proportional to δ. To identify the transition from mass to heat transfer control, we divide Eq. (6) by Pe, and

take the limit of $\phi \to 0$ while realizing that $\phi/Pe \to$ constant in this limit. After some manipulations, we arrive at

$$\left.\frac{\phi}{Pe}\right|_{\phi\to 0} = \left(\frac{1-\exp\left[-H\theta_0/(1-\theta_0)\right]}{H(\exp\left(Pe_0\right)-1)} + Le\,(1-1/\gamma)H\right)\left(\frac{1}{\theta_0}\right)$$
$$\equiv \frac{\phi_{crit}}{Pe_0}. \tag{8}$$

By plotting Pe/Pe_0 vs. ϕ/ϕ_{crit} we arrive at a set of similar curves for various thermodynamic and transport conditions of the system. These curves are presented in Fig. 2. The curves are based on thermodynamic property values for iodine (see Table 1), Lewis numbers of unity, $T_{C,0}/T_S = 0.95$, and Pe_0 of 0.01, 1, and 10. As expected, the curves asymptote to $Pe/Pe_0 \to 1$ and ϕ/ϕ_{crit} for $\phi/\phi_{crit} \gg 1$ and $\ll 1$, respectively, and the transition from mass to heat transfer control occurs for $\phi/\phi_{crit} \sim 1$. The behavior of the curves about $\phi/\phi_{crit} = 1$ is controlled primarily by Pe_0 – in that H, θ_0 and Le have only a higher–order effect. For relatively small values of Pe_0 this transition is gradual, whereas for large Pe_0 sharp break occurs between the two regimes.

One pertinent application of this model is a prediction of the crystal thickness at which growth goes from mass to heat transfer control. A characteristic value of this thickness is obtained by setting $\phi = \phi_{crit}$. Using the iodine property values given in Table 1 and $Pe_0 = 1$, this would correspond to $\delta/L \approx 0.2$. Actual crystal thickness – ampoule length ratios on this order would not be unrealistic. The inclusion of crystal heat conduction into a more detailed modelling of PVT systems for this particular type of crystal would therefore be warranted.

2.2. Two dimensional heat/mass transfer model

Similar to Refs. [2, 3, 7], we retain a primitive variable (i.e., pressure and velocities) formulation of the continuity and momentum equations. The computational domain is again illustrated in Fig. 1. The following assumptions are applied:

1. The flow within the ampoule is axisymmetric.
2. Gravity (if present) is directed towards the source.
3. The carrier gas is completely rejected at the interfaces.
4. Soret and Dufour effects are neglected.
5. Transport properties (c_p, k_g, D_{AB}, and the dynamic viscosity μ) are constant.

Even though we seek steady–state solutions, we have adopted a transient numerical formulation of the governing differential equations. Our rationale is that the transient approach avoids many of the problems associated with the direct, iterative solution of the steady–state equations – such as insuring global mass conservation at each iteration

stage [3, 10]. With the given assumptions, the governing equations for continuity, momentum, energy, and species in the vapor phase region are

$$\frac{\partial \rho}{\partial t} + \frac{1}{r}\frac{\partial \rho r v}{\partial r} + \frac{\partial \rho u}{\partial z} = 0 \tag{9}$$

$$\frac{\partial \rho v}{\partial t} + \frac{1}{r}\frac{\partial \rho r v^2}{\partial r} + \frac{\partial \rho u v}{\partial z} = -\frac{\partial P}{\partial r} + \frac{1}{r}\frac{\partial r \tau_{rr}}{\partial r} + \frac{\partial \tau_{rz}}{\partial z} - \frac{\tau_{\phi\phi}}{r} \tag{10}$$

$$\frac{\partial \rho u}{\partial t} + \frac{1}{r}\frac{\partial \rho r u v}{\partial r} + \frac{\partial \rho u^2}{\partial z} = -\frac{\partial P}{\partial z} + \frac{1}{r}\frac{\partial r \tau_{rz}}{\partial r} + \frac{\partial \tau_{zz}}{\partial z} - \rho g \tag{11}$$

$$\frac{\partial \rho T}{\partial t} + \frac{1}{r}\frac{\partial \rho r v T}{\partial r} + \frac{\partial \rho u T}{\partial z} = \frac{k_g}{c_p}\left(\frac{1}{r}\frac{\partial}{\partial r} r \frac{\partial T}{\partial r} + \frac{\partial^2 T}{\partial z^2}\right) \tag{12}$$

$$\frac{\partial \rho w_B}{\partial t} + \frac{1}{r}\frac{\partial \rho r v w_B}{\partial r} + \frac{\partial \rho u w_B}{\partial z} = D_{AB}\left(\frac{1}{r}\frac{\partial}{\partial r}\rho r \frac{\partial w_B}{\partial r} + \frac{\partial}{\partial z}\rho \frac{\partial w_B}{\partial z}\right), \tag{13}$$

in which

$$\tau_{rr} = \mu\left[2\frac{\partial v}{\partial r} - \frac{2}{3}\left(\frac{1}{r}\frac{\partial r v}{\partial r} + \frac{\partial u}{\partial z}\right)\right] \tag{14}$$

$$\tau_{rz} = \mu\left(\frac{\partial v}{\partial z} + \frac{\partial u}{\partial r}\right) \tag{15}$$

$$\tau_{zz} = \mu\left[2\frac{\partial u}{\partial z} - \frac{2}{3}\left(\frac{1}{r}\frac{\partial r v}{\partial r} + \frac{\partial u}{\partial z}\right)\right] \tag{16}$$

$$\tau_{\phi\phi} = \mu\left[2\frac{v}{r} - \frac{2}{3}\left(\frac{1}{r}\frac{\partial r v}{\partial r} + \frac{\partial u}{\partial z}\right)\right]. \tag{17}$$

In the above, ρ, P, and T are the density, total pressure, and temperature of the mixture, u and v are the z and r components of the mass–averaged velocity, and w_B is the mass fraction of the carrier species. We pose the species equation in w_B, rather than the common practice of $w_A = 1 - w_B$, for numerical reasons which will be described in the following section. We assume ideal behavior of the gas mixture,

$$P = \frac{\rho R_u T}{M}, \tag{18}$$

in which the average molecular mass M is given by

$$M = \left[\frac{1 - w_B}{M_A} + \frac{w_B}{M_B}\right]^{-1}. \tag{19}$$

The surface temperature of the source is taken to be uniform at T_S. The crystal surface temperature, on the other hand, is not specified a priori. Rather, we predict the crystal surface temperature by applying the conduction equation to the layer of crystal

material, again of thickness δ. Specifically, within the crystal the temperature (denoted as T_C) is governed by

$$\rho_s c_{p,s} \frac{\partial T_C}{\partial t} = k_s \left(\frac{1}{r} \frac{\partial}{\partial r} r \frac{\partial T_C}{\partial r} + \frac{\partial^2 T_C}{\partial z^2} \right). \tag{20}$$

Assuming that the crystal/vapor interface is stationary and planar (i.e., not significantly deformed from a z = constant surface) the interface boundary condition is

$$k_s \frac{\partial T_C}{\partial z} = k_g \frac{\partial T}{\partial z} - \rho u h_{sg}, \quad \text{at } z = L, \tag{21}$$

in which the latent enthalpy of species A, h_{sg}, is now on a unit mass basis. The temperature on the ending wall is taken to be uniform at the value $T_{C,0}$.

As before, we set the partial pressure of the nutrient vapor at the crystal/vapor interfaces to the local saturation pressure. The boundary conditions at the source are then given by

$$w_B(r,0,t) = 1 - \frac{M_A P_{A,sat}(T_S)}{M_B P} \left[1 - \frac{P_{A,sat}(T_S)}{P} \left(1 - \frac{M_A}{M_B} \right) \right]^{-1} \tag{22}$$

$$v(r,0,t) = 0 \tag{23}$$

$$u(r,0,t) = \frac{D_{AB}}{w_B} \left. \frac{\partial w_B}{\partial z} \right|_{z=0}. \tag{24}$$

Completely analogous boundary conditions are obtained at the crystal interface. Note, however, that the saturation pressure P_{sat} at the interface will be a function of r – by virtue of the non–isothermal interface conditions. A specific relationship for the saturation pressure is presented in a following section.

Temperature boundary conditions at the side walls will depend upon the specifics of the furnace system used to heat the ampoule. Here we assume that the wall temperature distribution follows that designed for the NASA μg crystal growth furnace [11]. This system consists of three independent sections; a hot zone under which the wall temperature will be uniform at T_S; an adiabatic zone; and a cold zone with wall temperature of $T_{C,0}$. Consequently, the wall temperature boundary conditions are

$$\begin{aligned} T(R,z,t) &= T_S, \quad 0 \le z \le z_{hot} \\ \left. \frac{\partial T}{\partial r} \right|_{r=R} &= 0, \quad z_{hot} < z < z_{cold} \\ T(R,z,t) &= T_{C,0}, \quad z_{cold} \le z \le L + \delta, \end{aligned} \tag{25}$$

in which z_{hot} and z_{cold} are specified transition points between the furnace sections.

The boundary conditions for mass fraction and radial velocity at the side wall depend on the wall values of nutrient partial pressure and saturation pressure. For $P_A/P_{A,sat} < 1$ deposition does not occur and the boundary conditions are

$$v(R,z,t) = 0 \tag{26}$$

$$\left.\frac{\partial w_B}{\partial r}\right|_{r=R} = 0. \tag{27}$$

If, on the other hand, the calculations predict that $P_A/P_{A,sat} \geq 1$, we assume that deposition takes place. The boundary conditions will then become

$$w_B(R,z,t) = 1 - \frac{M_A P_{A,sat}[T(R,z,t)]}{M_B P}\left[1 - \frac{P_{A,sat}[T(R,z,t)]}{P}\left(1 - \frac{M_A}{M_B}\right)\right]^{-1} \tag{28}$$

$$v(R,z,t) = \frac{D_{AB}}{w_B}\left.\frac{\partial w_B}{\partial r}\right|_{r=R}. \tag{29}$$

The common no–slip boundary conditions ($u(z,R,t) = 0$) are applied at the wall, although it should be noted that wall temperature gradients can result in a thermal creep flow over the surface [10, 12]. Calculations here will be limited to conditions in which creep has a negligible effect on vapor transport. Finally, symmetry conditions are applied at the ampoule centerline ($r = 0$), which correspond to zero v and zero radial gradients of u, T and w_B.

The system is initially taken to be at equilibrium at the crystal temperature $T_{C,0}$. Starting from $t = 0$, the temperature T_S is increased to the specified steady state value within a time period of t_c, which was typically taken to be 0.1 s. The initial conditions and the transient heating process were chosen simply to fascilitate the calculation of the steady state condition in the ampoule.

The final variable to be considered is the total pressure in the ampoule. Because velocities are specified at all surfaces, closure of the momentum and continuity equations alone do not require a unique specification of the pressure within the ampoule. That is, solution of these equations (for a fixed density field) will yield velocities u and v and a relative pressure distribution $P'(r,z,t)$ in the ampoule. However, the total (or absolute) pressure distribution in the ampoule, at any point in time, is needed to calculate the density from Eq. (18). To determine the total pressure, we first adjust P' by a constant so that the spacial average of P' is zero. The total pressure is then obtained from P' plus the mean absolute pressure P_m,

$$P(r,z,t) = P_m(t) + P'(r,z,t). \tag{30}$$

The value of $P_m(t)$ can be determined from total mass conservation within the ampoule. Integration the continuity equation over the ampoule volume yields

$$\frac{d}{dt}\int_0^L \int_0^R \rho\, r\, dr\, dz = \int_0^R (\rho u|_{z=0} - \rho u|_{z=L})\, r\, dr - R\int_0^L \rho\, v|_{r=R}\, dz. \qquad (31)$$

The density can be eliminated using the ideal gas law, Eq. (18), in which P would be given by Eq. (30). The above equation will then yield a relation for the change in mean pressure P_m as a function of u, v, P', T and w_B.

2.3. Numerical method

We have employed the popular and well–established SIMPLE algorithm to calculate the flow and pressure fields. The discretization of the continuity and momentum equations follows the staggered–grid procedure required by the SIMPLE method [13], and the control volume approach was used to discretize the species equation and the gas and solid phase energy equations. The interface conductivity method was used in the energy control volumes adjacent to the gas/crystal interface [13], with the latent heat contribution appearing as a source term. Time discretization was performed using a fully–implicit, forward–difference scheme. We use the discretized form of Eq. (31), combined with Eq. (18), to calculate the mean pressure P_m at each time step, and then use Eqs. (30) and (18) to re–calculate the density within the ampoule. Note that this scheme provides a density field that identically satisfies global mass conservation for an arbitrary velocity field. This behavior is critical for the convergence of the SIMPLE algorithm.

A subtle aspect in the numerical solution of the PVT system – which relates to our reason for using w_B as the species variable – regards the proper application of the mass fraction boundary conditions at the solid/vapor interfaces. The mass fraction of the carrier is specified on the interfaces – yet the total flux of carrier (diffusive and convective) is also specified, i.e., zero. It is essential to maintain this latter condition during the iterative solution of the discretized species equation. Otherwise, the total mass of carrier will change in time – which is physically impossible. To meet this condition, it is necessary to discretize the transient and convective terms in the species equation in a divergent form (which corresponds to the form of Eq. (13)), as opposed to the conservative form recommended by Patankar [13]. A consequence of this approach is that the interfacial values of mass fraction no longer explicitly appear in the discretized species equation. Rather, they become implicitly coupled to the species equation solely through the velocity boundary conditions, i.e., Eq. (24). Aside from this modification, iterative solution of the equations follows the procedure outlined by Patankar [13]. The steady state condition is established when the change in the variables from one time step to the next becomes negligible.

One drawback of the transient formulation is that it is not possible to specify beforehand the steady–state mean pressure of the PVT system. Rather, the steady–state value of P_m depends entirely on the specified initial and boundary conditions of the system. In situations in which the steady–state PVT behavior for a fixed P_m is desired, it is thus necessary to guess an initial charging pressure $P_{m,0}$ that will yield the sought final pressure. As expected, this process involves iteration between $P_{m,0}$ and the calculated P_m.

To verify our model we performed calculations to reproduce previous benchmark numerical investigations of two dimensional forced and free convective heat transfer in closed cavities [14, 15]. Further validation of our model was obtained by comparing results for PVT velocity fields and growth rates to those calculated in Refs. [2, 3, 7]. The calculated velocities and growth rates were found to be in acceptable agreement (ca. 5%) with the previous works.

3. Results and Discussion

3.1. System parameters

To be consistent with the previous modelling efforts in Refs. [2, 3, 7], we focus our attention on the H_2–I_2 PVT system. Values of the parameters in the PVT model that are fixed thoughout this investigation are given in Table 1. The equilibrium partial pressure of I_2 vapor was given by the relation [16]

$$P_{A,sat} = 101.32 \times 10^3 \exp\left(30.795 - \frac{8088.64}{T} - 2.013 \ln T\right) \quad \text{Pa.} \tag{32}$$

From the Clausius–Clayperon equation, the latent enthalpy of the vapor at a characteristic interface temperature of 360 K is calculated from the above as $h_{sg} = 2.64 \times 10^5$ J/kg, which agrees well with the value of 2.46×10^5 J/kg used by Abernathy et al. [8]. The initial charging pressure of the system (i.e., the pressure when the system is at equilibrium at $T_{C,0}$) was set to 10 kPa. This resulted in a final steady–state pressure within 10% of 13.3 kPa (100 torr) for all conditions examined.

Using these parameters and the conditions of zero gravity and isothermal interfaces, a grid dependence study revealed that the differences between the calculated steady–state growth rates for uniform 12×12 and 22×22 grids (in the gas phase region) were normally within 3 percent, and the difference between 22×22 and 42×42 grids was within 1 percent. All the results presented here were calculated with the 22×22 grid. Depending on the thickness of the crystal, between 5 and 10 rows of grid points were used in the discretization of the solid–phase energy equation.

3.2. Effect of conduction in crystal

Results of our calculations for combined solid and gas phase transport appear in Figs. 3 and 4, in which we present distributions of steady–state mass flux at the crystal surface for a solid thermal conductivity of $k_{sol} = 0.5$ W/m·K (solid iodine), with the crystal thickness δ randing from 0 to 5 mm. Results are given for zero gravity and unity gravity pointing towards the source (convectively stabilized). Figure 3 has a fixed side wall temperature of $T_{C,0}$ in the crystal region, whereas the crystal side walls for Fig. 4 are adiabatic. For all cases the temperature of the side walls in the gas–phase region ($0 \leq z \leq L$) was T_S, and the length L of the vapor region was fixed at 2 cm. A constant value of L would be expected since growth of the crystal layer would be balanced by regression of the source layer. For the zero crystal thickness, zero gravity case one sees the behavior identified by Greenwell et al. [7], in that flux is highest at the centerline, whereas stabilizing gravity results in a more uniform distribution for an isothermal interface as reported by Markham et al. [2].

A quick inspection of the curves in Figs. 3 and 4 reveals that the thermal boundary conditions on the side walls of the crystal can have a profound effect on the flux distribution. The constant temperature case (Fig. 3) is discussed first. As δ increases, the flux for both gravity conditions decreases at the centerline and dramatically increases at the wall. The behavior at the centerline follows from the one dimensional analysis in Sec. 2.1. Regions of the crystal near the centerline are cooled primarily by conduction to the end wall. Increasing the crystal thickness acts to increase the conduction resistance, and therefore increases the crystal surface temperature. The behavior near the wall, on the other hand, is somewhat counterintuitive. Regions of the crystal near the wall are thermally coupled to the side wall, and therefore maintain temperatures near $T_{C,0}$ regardless of the crystal thickness. Because of this, one might expect the flux at the wall to remain near the value predicted for zero crystal thickness – yet the flux actually increases with thickness. Transport mechanisms in the vapor phase are responsible for this behavior. The retardation of flux at the centerline acts to increase the nutrient concentration over the entire crystal, which in turn results in a higher concentration gradient – and mass flux – at the surfaces near the wall.

The flux distributions for zero and unit gravity are nearly identical at the maximum crystal thickness of 5 mm. Growth rates are now controlled primarily by solid phase conduction, and differences in the vapor–phase transport conditions (i.e., buoyancy or the lack thereof) will therefore have minimal effect of the flux distribution. When the crystal side wall is adiabatic (Fig. 4) the effect of wall cooling is removed, and the flux profiles attain a nearly uniform distribution. As before, increasing crystal thickness lessens the differences in flux distribution between the zero and unit gravity conditions.

The calculated flux profiles shown in Figs. 3 and 4 are essentially unaffected by the thermal boundary conditions at the side walls of the gas–phase region. For the given transport conditions the heat flux to the crystal interface is dominated by latent heat release from the depositing vapor. Gas–phase heat conduction from the heated side walls to the interface will therefore have a minimal effect on the interface temperature.

To illustrate the degree to which the interface can become nonisothermal, we plot in Fig. 5 interface temperatures as a function of radius for the same conditions as in Fig. 3. The variation in interface temperature for the $\delta = 5$ mm thickness is around 8 K across the 1 cm radius of the surface. Extremely high temperature gradients are predicted near the wall, which is a consequence of the large heat flux that results from latent heat release. Indeed, it seems unlikely that such conditions would be attained in practice, because the finite thermal conductivity of the wall material would result in wall temperatures somewhat elevated above the nominal values used here. Nevertheless, it is clear that the high heat fluxes resulting from vapor deposition can lead to significant temperature gradients within the crystal – especially when the side walls of the crystal are cooled.

The effect of crystal conduction heat transfer on the overall mass transfer rates is presented in Fig. 6. Here we adopt the normalization used in the 1–D analysis, and plot the ratio $Pe/Pe_{1-D,0}$ vs. ϕ/ϕ_{crit}, where Pe is the Peclet number calculated from the 2–D results and $Pe_{1-D,0}$ is that corresponding to the 1–D model with zero crystal thickness. The results are based on the isothermal crystal side wall, zero gravity configuration. Two sets of Peclet number ratios are presented, which correspond to Pe based on the mass averaged velocity and the centerline velocity. Also included are the 1–D analytical predicitions for the same thermal and transport parameters of the system.

The numerical results for Pe based on the centerline velocity are seen to correspond reasonably well with the 1–D preditions over the entire range of crystal thicknesses. This is to be expected, because the interface temperature at the centerline is, again, controlled primarily by the axial conduction of heat across the crystal. On the other hand, the increased flux at the crystal edges – which results from the inherently two–dimensional nature of energy transfer in the ampoule – leads to mass–averaged Pe values that are only slightly affected by increasing crystal thickness.

It is apparent from the preceeding results that heat transfer within a poorly conducting crystal can significantly affect the distribution of vapor deposition. The thermal boundary conditions on the side wall containing the crystal play a critical role in governing this distribution. Ideally, a uniform distribution would be sought, and this would be best realized by maintaining adiabatic side walls. This condition, however, is difficult to attain in practice [3]. Cooled side walls – which are more physically realistic – will eventually lead to a concave interface shape due to the preferential deposition of vapor at the crystal

edges. This has been observed experimentally by Abernathy et al. in the growth of iodine crystals in high Pe conditions [8].

3.3. Effect of wall deposition

To investigate the effects of wall deposition, we simply extended the cooled section of the side wall into the gas phase region. Results of the calculations appear in Fig. 7 and 8, in which mass flux is plotted vs. position for vapor–phase cold zone lengths ranging from $\Delta z_{cold} = 2$ to 10 mm. Figure 7 shows the flux at the interface (i.e., the intended target of deposition), whereas Fig. 8 shows the side wall flux. To focus solely on the effects of wall deposition, the end wall interface in both plots has been maintained at the uniform temperature of $T_{C,0}$. As before, results are given for zero and unit, stabilizing gravity.

The first point to draw from Fig. 7 is that wall deposition results in a significant decrease in overall mass transfer to the crystal interface. The side wall deposition surfaces, being closer to the source, act to scavenge nutrient vapor from the crystal. To quantify this effect, the 2 mm section of wall deposition surface results in an approximately 30 and 50% decrease in the total mass flux reaching the interface for the zero and unit gravity cases, respectively. Equally significant is the effect of side wall deposition on the distribution of flux at the interface. A 90 percent variation in flux across the radius of the interface occurs for $\Delta z_{cold} = 2$ mm, as opposed to around 10 percent variation in the absence of side wall deposition. Not surprizingly, the location of maximum flux in the entire ampoule occurs on the cooled side wall positions that are nearest to the source (Fig. 8) – simply because they are exposed to a relatively higher nutrient concentration.

Perhaps the most interesting aspect of side wall deposition are its effects on buoyant convection in stabilized configurations. Our calculations indicate that side wall deposition, in conjunction with source–directed gravity, can act to create a recirculation flow within the gas. The nature of the recirculation is shown in Fig. 9, in which we present vector plots of the mass averaged velocity for unit, source–directed gravity. To explain the behavior of the flow, we note, first, that the vapor density at the wall deposition surface will be lower than that at the immediately adjacent centerline – assuming, of course, that $M_A > M_B$. Gravity will therefore impart a relatively higher body force in the gas at the centerline. Concurrently, a radial convective flow will occur as the vapor is swept to the side wall deposition surfaces – and the magnitude of this flow will be greatest at the boundary between the cold and hot zones of the ampoule. Once the length of wall exceeds a critical value (around 5–6 mm for the ampoule conditions used here) the combined effects of radial density gradients and radial velocities result in a recirculating flow. The recirculation is counter to that attained in destabilizing gravity (i.e., g pointed towards the crystal), in that the flow is directed towards the source at the centerline and towards the crystal at

the wall. Referring again to Figs. 7 and 8, the recirculation acts to significantly lower the interface flux at the centerline, and increase the flux at the hot/cold junction of the wall, relative to the zero gravity condition.

We emphasise again that the recirculation shown in Fig. 9 results from a complicated interaction between the axial and radial–directed convective flow of the vapor and buoyancy forces. For example, regardless of the wall thermal conditions, removal of the Stefan flow (by setting normal velocities at all surfaces to zero) while maintaining all other conditions the same resulted in convectively stable systems for source–directed gravity. This is in contrast to unstable (crystal–directed) gravity, in which solutal density differences, by themselves, can result in convective recirculation within the ampoule [17].

5. Conclusions

Our calculations certainly indicate that an accurate modelling of PVT ampoules should include heat transfer in the crystal and (if present) deposition on the side walls. Both of these factors have been shown to significantly affect the rate and uniformity of crystal growth. We also submit that the results could have bearing on the effects of buoyant convection on the morphological stability of crystals grown in PVT ampoules. Again, significantly different distributions in flux between zero and unit–stablized gravity were observed in the presence of side wall deposition. A primary factor behind these differences is the fact that the growth interface, as a whole, becomes non–planar. Because of this, it is conceviable that a non–planar crystal interface would evolve differently under stablized gravity and zero gravity conditions – regardless of the presence of side wall deposition. An accurate prediction of such effects would require a numerical scheme that can conform to the non–planar boundary of the crystal. We are currently engaged in the modification of our model to account for such effects.

Acknowedgements:

This work was supported by NASA Microgravity Sciences and Applications Division Grant NAG-977, Benjamin Penn, Contract Administrator.

References

[1] F. E. Rosenberger, Fundamentals of Crystal Growth, (Springer, N.Y., 1979).

[2] B. L. Markham, D. W. Greenwell, and F. Rosenberger, J. Crystal Growth 51 (1980) 426.

[3] A. Nadarajah, F. Rosenberger, and J. I. D. Alexander, J. Crystal Growth 118 (1992) 49.

[4] H. Wiedemeier and D. Chandra, J. Crystal Growth 57 (1982) 159.

[5] M. K. Debe, R. J. Poirier, E. L. Cook, L. R. Miller, M. S. Spiering, and S. P. Floeder, J. Vac. Sci. Tech. A 8 (1990) 49.

[6] L. van den Berg and W. F. Schnepple, Nucl. Instr. Methods A 283 (1989) 335.

[7] D. W. Greenwell, B. L. Markham, and F. Rosenberger, J. Crystal Growth 51 (1980) 413.

[8] J. R. Abernathy, D. W. Greenwell, and F. Rosenberger, J. Crystal Growth 47 (1979) 145.

[9] O. A. Louchev and V. M. Zaletin, J. Crystal Growth 148 (1995) 125.

[10] D. G. Walker, D. W. Mackowski, and R. W. Knight, AIAA 32nd Aerospace Sciences Meeting and Exhibit, 10–13 January 1994, Reno, NV, paper 94–0567.

[11] Teledyne Brown Engineering, Document SP–DOC–6102, (1990).

[12] D. E. Rosner, Phys. Fluids A1 (1989) 1761.

[13] S. V. Patankar, Numerical Heat Transfer and Fluid Flow, McGraw-Hill, N.Y., 1980.

[14] U. Ghia, K. N. Ghia, and C. T. Shin, J. Computational Phys. 48 (1982) 387.

[15] G. deVahl Davis, Int. J. Num. Methods Fluids 3 (1983) 249.

[16] L. J. Gillespie and L. H. D. Fraser, Am. Chem. Soc. J. 58 (1936) 2260.

[17] J. C. Launay, J. Miroglio, and B. Roux, J. Crystal Growth 51 (1981) 61.

Table 1. Model parameters

M_A	254 g/mole
M_B	2 g/mole
D_{AB}	1.25 cm^2/s (@ 100 Torr)
μ	1.5×10^{-4} g/cm·s
$Pr\ (= c_p\mu/k_g)$	1
γ	1.4
$\overline{c}_p$	$3.5R_u$
T_S	378.1 K
$T_{C,0}$	358.1 K
R	1 cm
L	2 cm
k_s	0.5 W/m·K
h_{sg}	2.64×10^5 J/kg

Figure Captions

1. Ampoule schematic.
2. Ratio of 1–D Peclet numbers with and without solid phase heat transfer vs. dimensionless solid phase resistance parameter.
3. Local mass flux at crystal surface vs. radial position, isothermal crystal side wall.
4. Same as Fig. 3, except with adiabatic crystal side wall.
5. Interfacial surface temperature distribution for conditions of Fig. 3.
6. Ratio of Peclet numbers with and without solid phase heat transfer vs. dimensionless solid phase resistance parameter.
7. Local mass flux at crystal interface vs. radial position.
8. Local mass flux at side wall vs. side wall position. Conditions same as in Fig. 7.
9. Velocity vectors for case of Figs. 7 and 8, unit stabilizing gravity.

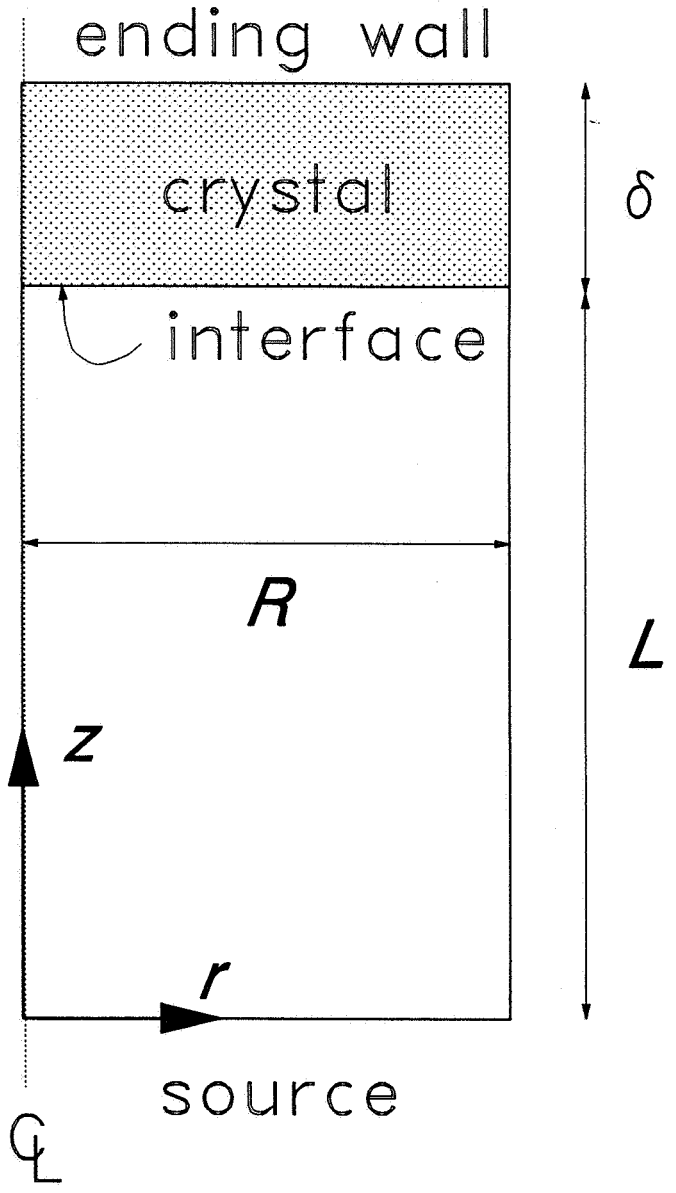

Fig. 1, Mackowski et al.

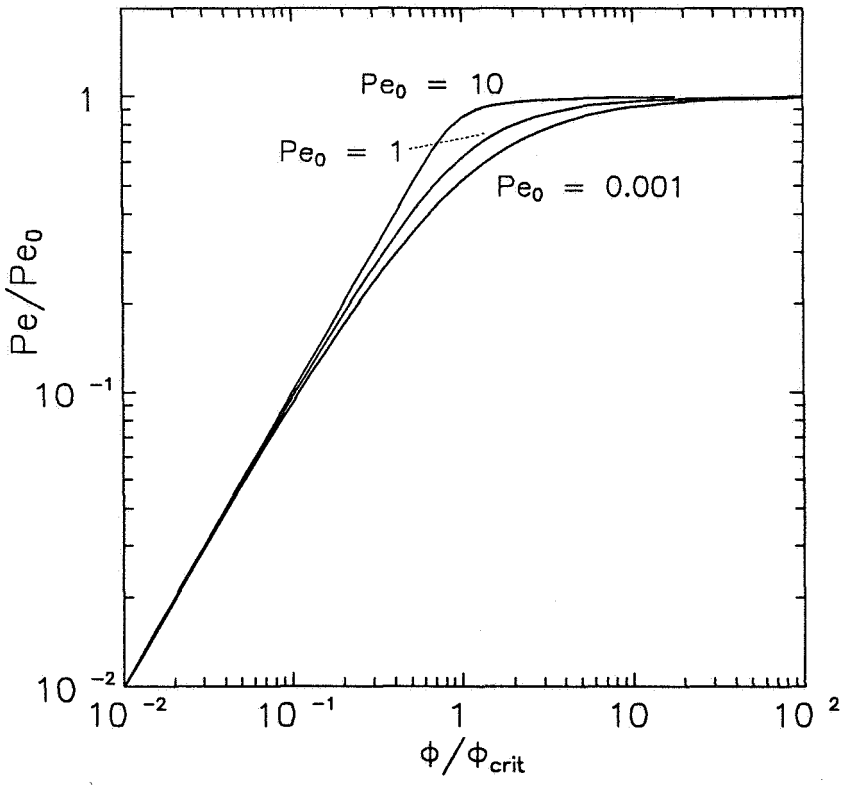

Fig. 2, Mackowski et al.

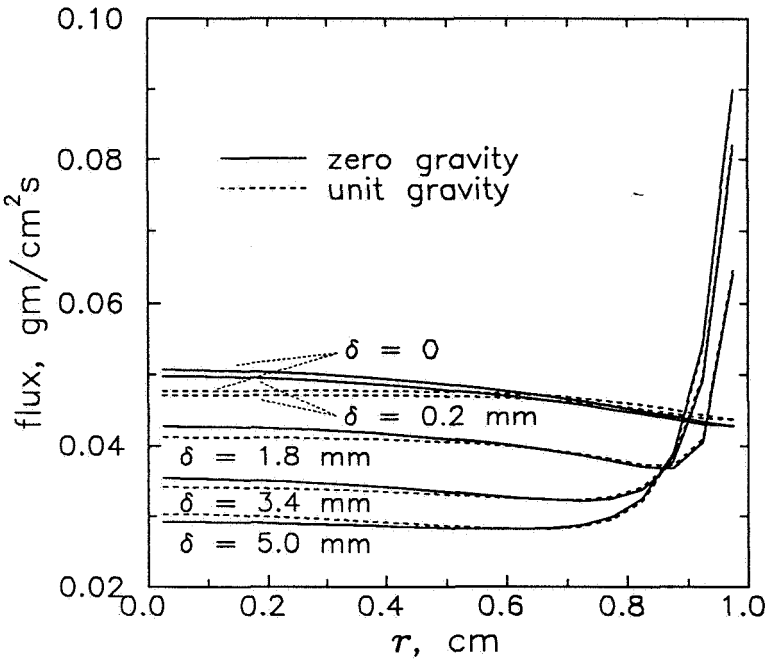

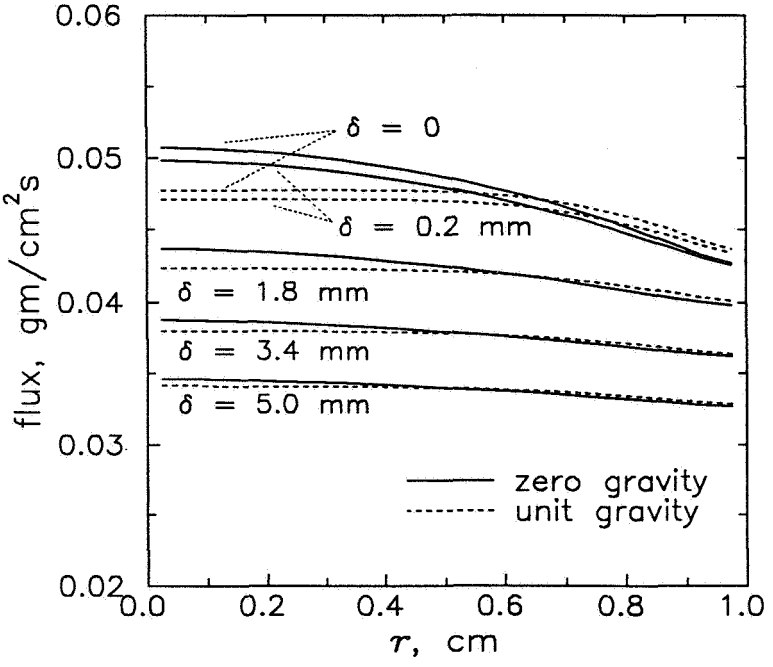

Figs. 3 & 4, Mackowski et al.

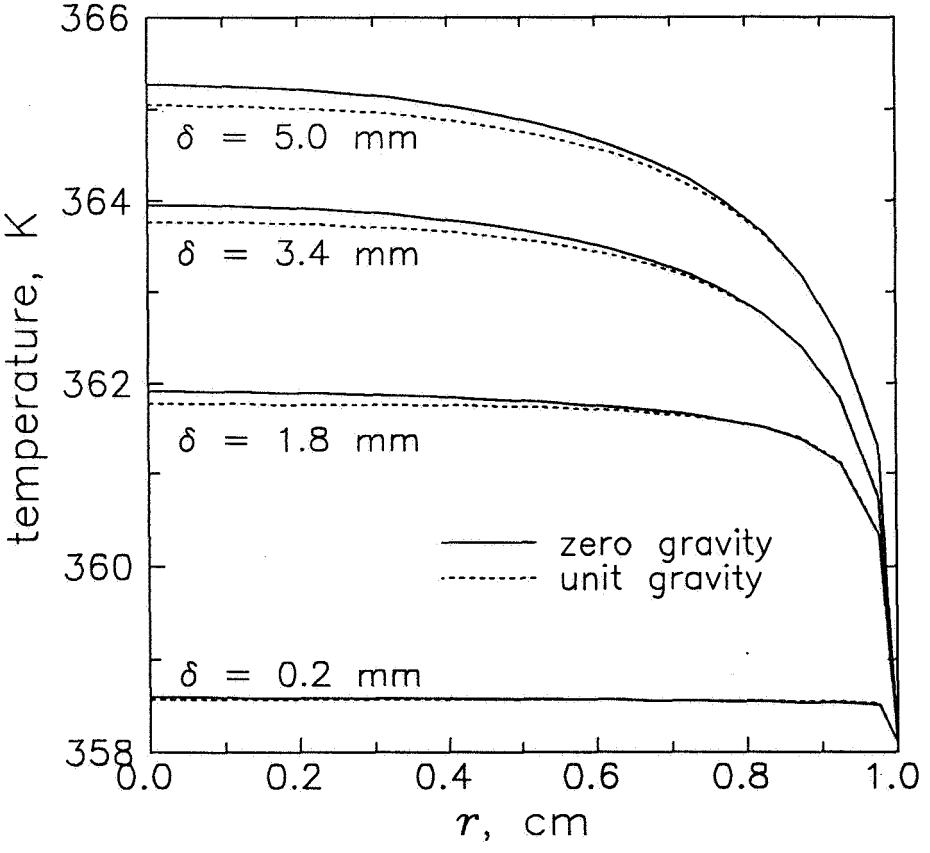

Fig. 5, Mackowski et al.

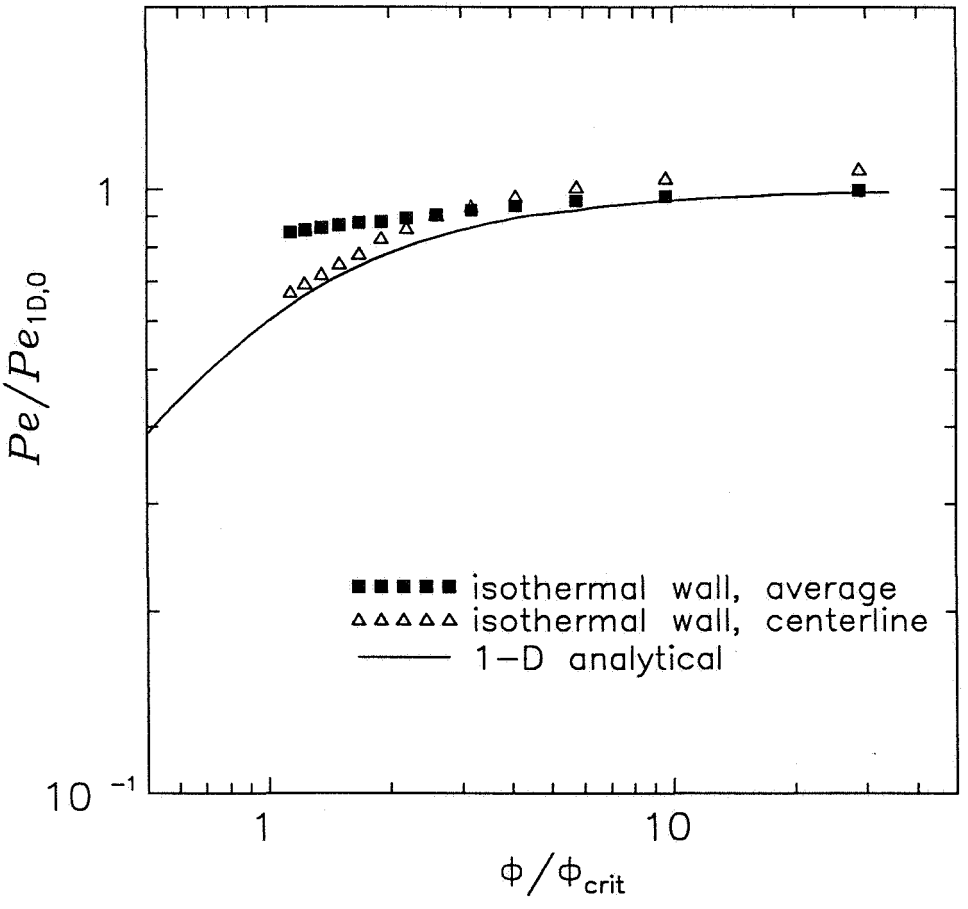

Fig. 6, Mackowski et al.

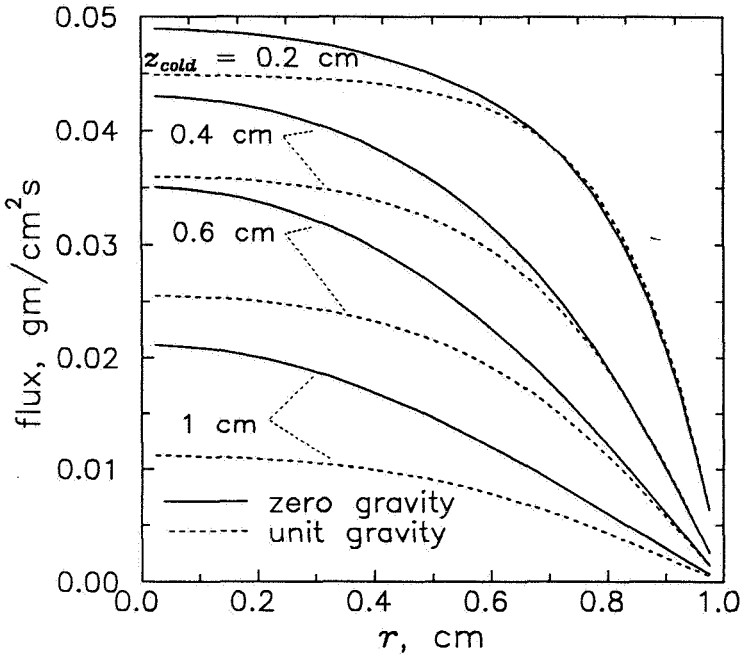

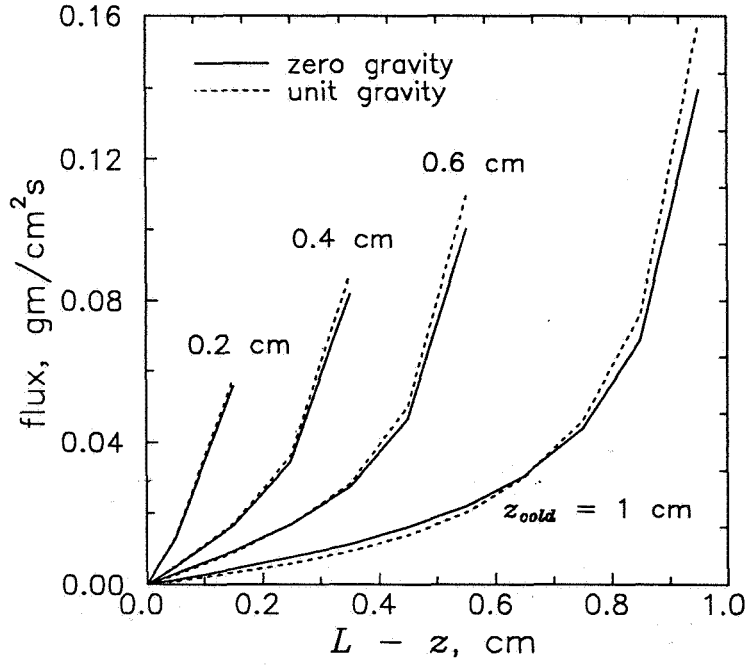

Figs. 7 & 8, Mackowski et al.

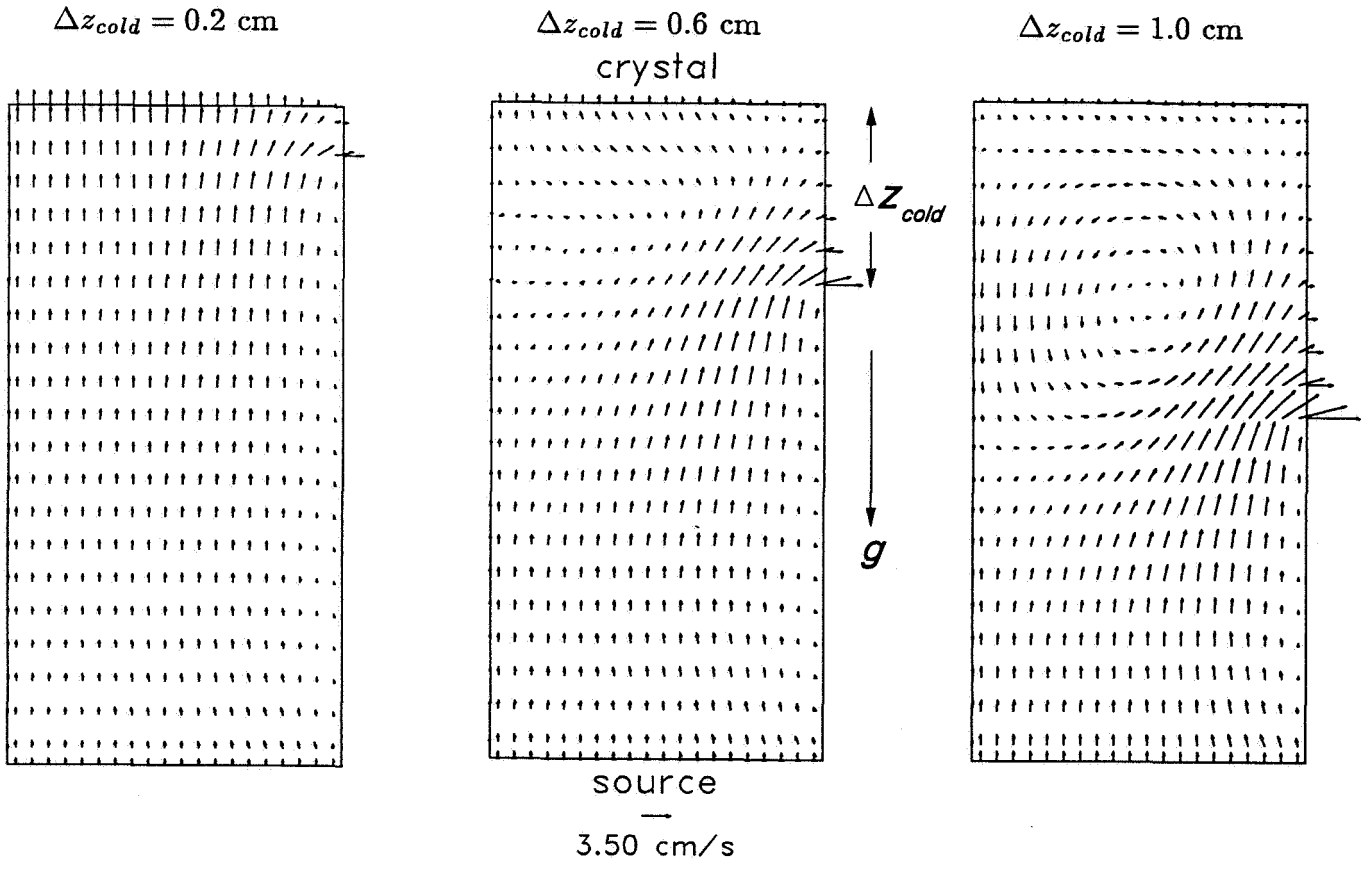

Fig. 9, Mackowski et al.